

Comparative study on the wake dynamics of pump-jet and ducted propeller based on dynamic mode decomposition

Citation for published version (APA):

Zhao, X., Shen, X., Geng, L., Zhang, D., & van Esch, B. P. M. (2023). Comparative study on the wake dynamics of pump-jet and ducted propeller based on dynamic mode decomposition. *Physics of Fluids*, 35(11), Article 115135. <https://doi.org/10.1063/5.0167130>

Document license:
TAVERNE

DOI:
[10.1063/5.0167130](https://doi.org/10.1063/5.0167130)

Document status and date:
Published: 01/11/2023

Document Version:
Publisher's PDF, also known as Version of Record (includes final page, issue and volume numbers)

Please check the document version of this publication:

- A submitted manuscript is the version of the article upon submission and before peer-review. There can be important differences between the submitted version and the official published version of record. People interested in the research are advised to contact the author for the final version of the publication, or visit the DOI to the publisher's website.
- The final author version and the galley proof are versions of the publication after peer review.
- The final published version features the final layout of the paper including the volume, issue and page numbers.

[Link to publication](#)

General rights

Copyright and moral rights for the publications made accessible in the public portal are retained by the authors and/or other copyright owners and it is a condition of accessing publications that users recognise and abide by the legal requirements associated with these rights.

- Users may download and print one copy of any publication from the public portal for the purpose of private study or research.
- You may not further distribute the material or use it for any profit-making activity or commercial gain
- You may freely distribute the URL identifying the publication in the public portal.

If the publication is distributed under the terms of Article 25fa of the Dutch Copyright Act, indicated by the "Taverne" license above, please follow below link for the End User Agreement:

www.tue.nl/taverne

Take down policy






If you believe that this document breaches copyright please contact us at:

openaccess@tue.nl

providing details and we will investigate your claim.

RESEARCH ARTICLE | NOVEMBER 21 2023

Comparative study on the wake dynamics of pump-jet and ducted propeller based on dynamic mode decomposition

Xutao Zhao (赵旭涛) ; Xi Shen (沈熙) ; Linlin Geng (耿琳琳); Desheng Zhang (张德胜)  ;
B. P. M. (Bart) van Esch 



Physics of Fluids 35, 115135 (2023)

<https://doi.org/10.1063/5.0167130>



View
Online



Export
Citation

Physics of Fluids

Special Topic:

John Michael Dealy (1937-2024): Celebrating His Life

Guest Editors: Alan Jeffrey Giacomini and Savvas G. Hatzikiriakos

[Submit Today!](#)

Comparative study on the wake dynamics of pump-jet and ducted propeller based on dynamic mode decomposition

Cite as: Phys. Fluids **35**, 115135 (2023); doi: 10.1063/5.0167130

Submitted: 10 July 2023 · Accepted: 3 November 2023 ·

Published Online: 21 November 2023



View Online



Export Citation



CrossMark

Xutao Zhao (赵旭涛),¹ Xi Shen (沈熙),¹ Linlin Geng (耿琳琳),¹ Desheng Zhang (张德胜),^{1,a)} and B. P. M. (Bart) van Esch²

AFFILIATIONS

¹Research Center of Fluid Machinery Engineering and Technology, Jiangsu University, Zhenjiang 212013, China

²Department of Mechanical Engineering, Eindhoven University of Technology, Eindhoven 5600MB, The Netherlands

^{a)}Author to whom correspondence should be addressed: zds@ujs.edu.cn

ABSTRACT

A comparative study on the wake dynamics of a pump-jet propulsor (PJP) and a ducted propeller (DP) is conducted to investigate the effects of the pre-swirl stator and corresponding stator-rotor interaction on the wake evolution and destabilization mechanisms of a PJP system. The flow field analysis, vortex structure identification, and dynamic mode decomposition (DMD) analysis are carried out based on the numerical results obtained from delayed detached eddy simulations. The numerical hydrodynamic loading and flow field of the PJP are compared with experimental results, and they are in good agreement. Compared with the DP, the stator trailing vortices of the PJP interact with the rotor trailing vortices as well as the hub vortex, accelerating their diffusion and viscous dissipation. The pre-swirl stator triggers the generation of secondary vortices and moderates the spiral behavior of tip leakage vortices, which dominates the wake instability of PJP. The DMD analysis revealed that the wake field evolution is primarily characterized by the different mode structures at blade passing frequency and its multiples, especially in the PJP due to its strong stator-rotor interaction. The modal energy decays faster in the PJP wake field owing to its more turbulent and earlier instability. The hub vortex plays an important role in the wake dynamics of the DP.

Published under an exclusive license by AIP Publishing. <https://doi.org/10.1063/5.0167130>

I. INTRODUCTION

The wake field commonly exists behind the rotor systems operating in a freestream, such as ship propellers and wind turbines, which contains complicated vortical structures evolving from near field to far field in a complex physical behavior.¹⁻³ In the case of propeller propulsion systems, the evolution of turbulent wake structures plays a crucial role in determining the hydrodynamic and hydroacoustic performance of the system.⁴⁻⁶ A pump-jet propulsor (PJP) is a complex multi-component propulsor including a duct, a rotor, and a stator, which is primarily used in underwater vehicles. Compared with regular propellers and ducted propellers (DP), the PJP features more complex wake coherence structures and uniquely wake destabilizing evolution mechanism under the modulation of strong rotor-stator interaction, which is challenging for its engineering design.⁷⁻⁹

The wake dynamics of the isolated marine propellers has been studied theoretically and experimentally since the early 20th century.^{3-5,10,11} A regular propeller with N blades operating in the axisymmetric flow usually includes N tip vortices, N trailing edge vortices and

one hub vortex. These vortex structures undergo different modes of mutual interaction as they evolve downstream until completely destabilize and disintegrate.¹ Widnall¹⁰ theoretically proposed three models of instability evolution for helical vortex filaments, they are short-wave instability model, long-wave instability mode and mutual-inductance mode, which are helpful for understanding the propeller wake instabilities. Felli *et al.*⁵ studied the wake evolution of open propellers with different blade numbers by means of high-speed visualizations and velocity signal measurements. They found that there is possible cause-effect relationship between the destabilization of the tip vortices and hub vortex, and the transition to instability of tip vortices is more related to the spiral-to-spiral interaction. The computational fluid dynamics (CFD) techniques are becoming popular to study propeller wake dynamics with the upgrading of computational software and hardware. Several works compared the capabilities of different turbulence modeling in resolving the wake vortex structures.¹²⁻¹⁴ Compared to the Reynolds-averaged Navier-Stokes (RANS) simulation, detached eddy simulation (DES) and large eddy simulation (LES) are able to

resolve the detailed three-dimensional wake vortex structures and capture their spatial-temporal evolution.^{14,15} Kumar and Mahesh¹ performed well-resolved LES to study the evolution mechanisms of propeller wake and pointed out that the preferred mechanism of propeller wake instability is strongly dependent on blade geometry and operating conditions. The mutual inductance between the rolled-up trailing edge wake and the tip vortices is the primary mechanism causing the wake instability in their study. Posa *et al.*¹⁶ observed the wake characteristics of a submarine propeller are mainly dominated by tip and hub vortices, and also verified load conditions substantially affect the wake structures. When a propeller is surrounded by a duct, known as a ducted propeller, the intensity of tip vortices largely depends on the clearance size between the blade tip and the duct, and the shear vortex shedding from duct external surface will further interact with the tip vortices and thereby cause numerous secondary coherent vortex structures.¹⁷ This indicates that the wake characteristics of the DP are to some extent different from those of the single propellers. Gong *et al.*¹⁸ conducted a comparative numerical analysis on the wake dynamics of ducted and non-ducted propellers. They found that the interaction between the duct and the propeller directly changes the topography of the wake vortex and the corresponding energy distribution. Zhang and Jaiman¹⁹ observed the short-wave instability is the primary mechanism for tip vortex destabilization of a four-bladed DP, followed by the secondary vortex system.

The wake dynamics of the PJP is becoming increasingly attractive due to its close relationship with the excitation and hydroacoustic characteristics of the propulsion system. However, most of the studies on PJP wake dynamics concentrated on numerical analysis due to the challenging of experimental investigations. Li *et al.*⁸ studied the wake instabilities of a PJP with pre-swirl stator in open water conditions via DES turbulent modeling. The wake coherent structures are identified by the omega criterion and divided into two interaction systems, one is the interaction between the tip leakage vortex (TLV) and the duct shedding vortex (DSV) and the other is the interaction between the stator trailing vortex (STV), the rotor trailing vortex and the hub vortex. It is also found that there is a really weak correlation between the TLV and the destabilization of the hub vortex, which is different from the wake evolution mechanism of a single propeller studied by Felli *et al.*⁵ Qin *et al.*⁷ investigated the effects of the parity of rotor and stator blades on the vortex destabilizing mechanisms of the PJP. The instability of the TLV is found to be more related to the number of rotor blades which determines the spiral-to-spiral distance. Yu *et al.*²⁰ studied the effects of stator parameters including pre-swirl angle, the rotor–stator spacing and the blade chord length on the propulsion performance of a PJP. Li *et al.*^{21,22} observed that the blade angles and circumferential arrangement spacing of stator affect both thrust fluctuation and vortex structure evolution of the PJP system. It is concluded from the literature that the existence of the stator in PJP system brings the strong stator–rotor interaction, resulting in its wake topology and evolution mechanism is significantly different from that of a normal propeller. It is valuable to investigate the effect of stator and stator–rotor interaction on the PJP wake dynamics from a fluid physics perspective.

Modal decomposition techniques are able to effectively extract the dominant coherent structure of the flow field from massive spatial-temporal data obtained by experimental measurements or numerical simulations, which are widely used in analyzing the rotor wake

structures.^{23–28} The proper orthogonal decomposition (POD)²⁹ and dynamic mode decomposition^{30,31} (DMD) are the most popular ones. Magionesi *et al.*²³ investigated the evolution and destabilization mechanisms of the propeller wake by analyzing the spatial shape of the modes in different characteristics frequencies obtained from POD and DMD. The effectiveness of the two approaches in identifying the underlying temporal and spatial scales of the wake flow is also compared. Shi *et al.*^{24,25} employed POD and DMD to decompose the vorticity magnitude in the core wake region of a propeller with or without a duct. They concluded that both methods can provide the most representative subset of modes to explore the wake destabilization mechanisms. It is also highlighted that the POD modes can be totally covered by the DMD results and the various orders of DMD modes are more convenient for seeking physical causes due to their single frequency characteristics. Zhi *et al.*³² employed DMD to decompose and reconstruct the transient propeller wake field in order to develop a reduced-order model for predicting the propeller wake. Wang *et al.*^{33–35} found that the morphology of wake flow structures of DMD modes at different frequencies largely characterizes the instability process of the propeller wake system. Most of the modal analysis on the wake field of marine propulsion systems are focused on single propellers and DPs, and there is less work performed on PJP systems according to the best of our knowledge. It is worthwhile to study the wake dynamics of PJP by using modal analysis technique.

In this study, the delayed detached eddy simulation (DDES) is carried out to comparatively study the wake dynamics of DP and PJP in a pure axial flow. The flow field analysis, vortex structure identification and DMD analysis are applied to investigate the effects of pre-swirl stator and corresponding stator–rotor interaction on the wake dynamics and destabilization mechanisms of a PJP system. The objectives of the present work are as follows: (i) By comparing the wake characteristics of DP and PJP to understand the modulation effect of the pre-swirl stator on PJP wake flow, thereby further guide the stator–rotor matching design. (ii) The coherent wake structures of PJP are more complicated than that of single propeller and DP, it is of interest to extract the dominant structures in the PJP wake field by the DMD analysis, and thereby investigate the wake instability mechanism of PJP system. The paper is structured as follows: The numerical methodology is shown in Sec. II; The wake field analysis of PJP and DP cases is shown in Sec. III; The dynamic mode decomposition analysis for wake field is presented in Sec. IV, and the conclusions are drawn in Sec. V.

II. NUMERICAL METHODOLOGY

A. Governing equations

Unsteady numerical simulations are carried out on the three-dimensional flow field of the DP and PJP systems based on the DDES modeling. The incompressible mass and momentum conservation equations are shown as follows:

$$\frac{\partial \rho}{\partial t} + \frac{\partial(\rho u_j)}{\partial x_j} = 0, \quad (1)$$

$$\begin{aligned} & \frac{\partial(\rho u_i)}{\partial t} + \frac{\partial(\rho u_i u_j)}{\partial x_j} \\ & = -\frac{\partial p}{\partial x_i} + \frac{\partial}{\partial x_j} \left[\mu + \mu_t \left(\frac{\partial u_i}{\partial x_j} + \frac{\partial u_j}{\partial x_i} - \frac{2}{3} \frac{\partial u_k}{\partial x_k} \delta_{ij} \right) \right], \quad (2) \end{aligned}$$

TABLE I. Pre-swirl stator PJP parameters.

Description	Value
Rotor diameter D	166.4 mm
Hub diameter ratio D_h/D	0.3
Tip clearance δ	1 mm
Rotor blade number Z_r	6
Stator blade number Z_s	8
Rotor–stator spacing	0.35D
Basic blade section	NACA66
Rotation speed n	20 rps

where ρ is the density, u_i is the velocity vector, p is the pressure, μ is the dynamic viscosity, and μ_t is the turbulent eddy viscosity.

The DDES is a cost-effective hybrid RANS/LES turbulence modeling approach. It covers the boundary layer by a RANS model and switches to a LES mode in highly separated regions, and overcomes the grid induced separation problem in the original DES model.³⁶ This model offers good prediction accuracy for transient vortex evolutions of propellers and PJPs.^{23–25} The governing equations of it are as follows:³⁶

$$\frac{\partial(\rho k)}{\partial t} + \frac{\partial(\rho k u_j)}{\partial x_j} = \frac{\partial}{\partial x_j} \left[\left(\mu + \frac{\mu_t}{\sigma_{k3}} \right) \frac{\partial k}{\partial x_j} \right] + P_k - \frac{\rho k^{3/2}}{l_{DDES}}, \quad (3)$$

$$\frac{\partial(\rho \omega)}{\partial t} + \frac{\partial(\rho \omega u_j)}{\partial x_j} = \frac{\partial}{\partial x_j} \left[\left(\mu + \frac{\mu_t}{\sigma_{\omega 3}} \right) \frac{\partial \omega}{\partial x_j} \right] + \alpha_3 \frac{\omega}{k} P_k - \beta_3 \rho \omega^2 + 2(1 - F_1) \rho \frac{1}{\omega \sigma_{\omega 2}} \frac{\partial k}{\partial x_j} \frac{\partial \omega}{\partial x_j}, \quad (4)$$

where the k equation is developed from shear stress transport (SST) $k-\omega$ turbulence model by adding the length scale term l_{DDES} , which is expressed as

$$l_{DDES} = l_{RANS} - f_d \max(0, l_{RANS} - l_{LES}), \quad (5)$$

where f_d is an empirical delay function, $l_{RANS} = \sqrt{k}/C_\mu \omega$, and $l_{LES} = C_{DES} \Delta_{max}$. The C_{DES} is calculated with the function: $C_{DES} = C_{DES1} \cdot F_1 + C_{DES2} \cdot (1 - F_1)$, where F_1 is the blending function. Some constants are: $C_\mu = 0.09$, $C_{DES1} = 0.78$, and $C_{DES2} = 0.61$.

B. Numerical setups

In this study, a scaled PJP model is considered as the research object, which includes a pre-swirl stator with 8 blades, an axial flow rotor with 6 blades, and a decelerating duct. The main geometric parameters of the PJP model are presented in Table I, and the actual configurations are shown in Fig. 1. The rotor diameter D is 166.4 mm, and the hub diameter ratio D_h/D is 0.3, where D_h is the diameter of rotor hub. The tip clearance of rotor is designed as 1 mm. The basic blade section of rotor and stator is NACA66 airfoil. The axial distance between the stator and rotor is 0.35D. The DP model is obtained by removing the stator blades from the PJP, as shown in Fig. 1(b). The PJP model is also machined to carry out hydrodynamic tests to validate the numerical simulations, as shown in Fig. 1(c). For the operating condition, both the PJP and DP models are operating with a fixed rotation speed $n = 20$ rps at the design advance coefficient $J = U/nD = 1.0$, where U is the inflow velocity.

Figure 2 shows the computational domain details. The entire computational domain is divided into several subdomains, including far field domain, near field domain, rotor domain and stator domain (for the PJP model only). The far field domain is a cuboid with rounded corners, has a size of $16D \times 3.6D \times 3.6D$, which is same as the dimension of the experimental water tunnel. The blockage ratio of the far field domain ($\lambda = A_d/C = 0.06$, where A_d is the disk area of rotor and C is the area of test-section cross section) is less than the rule of thumb ($\lambda < 0.1$) suggested in Ref. 1, thereby the evolution of rotor wake is negligibly affected by the domain size. The near field domain is separated out to refine the mesh distribution of the wake field, with a cylinder of diameter $2D$ and length $5.5D$.

The entire computational domain is discretized by the hexahedral meshes, where the rotor domain discretization is completed in Turbogrid software, and the other domains are discretized by using ICEM CFD software. Three mesh schemes with different mesh densities are set to carried out the mesh independent test for the PJP model, including coarse mesh scheme (4.98×10^6), medium mesh scheme (9.38×10^6), and fine mesh scheme (20.18×10^6). The grid convergence index (GCI) proposed by Celik *et al.*³⁷ is also used to estimate the discretization error for PJP case in two different advanced coefficients $J = 0.6$ and $J = 1.0$, the detailed results can be found in our previous work.³⁸ Considering the computational cost and the flow field resolution level, the fine mesh scheme is finally selected to carried out

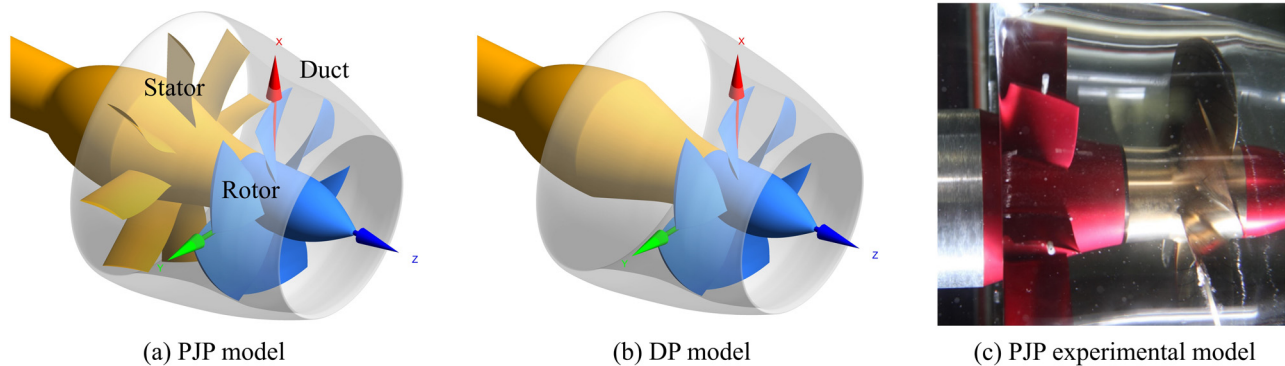


FIG. 1. The 3D geometries of PJP and DP models.

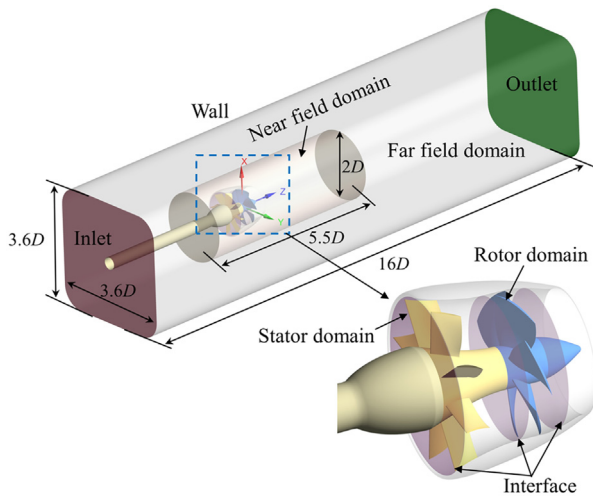


FIG. 2. The computational domain of PJP model.

the wake flow simulation. To ensure comparable results, the DP case is assigned a similar mesh number to that of the PJP case, totaling 19.32×10^6 elements. Figure 3 illustrates the mesh distribution details of the fine mesh scheme, where Fig. 3(a) provides a global overview of mesh distribution for the PJP model, Figs. 3(b)–3(d) zoom in on mesh distribution surrounding the rotor blade and tip clearance. It is important to note that 30 grid nodes are placed in the rotor’s tip clearance.

Figures 3(e) and 3(f) show the mesh distribution in the wake region, with mesh refinement focused around the generation zones of the tip vortex and hub vortex. For PJP and DP cases, the average y^+ for rotor blade, stator blade (for the PJP model only) and duct surface are 2.6, 2.8, and 1.8, respectively.

The simulation commences with the calculation of the steady flow solution using the traditional Moving Reference Frame (MRF) method, coupled with the SST $k-\omega$ turbulence model. Velocity inlet and pressure outlet boundary conditions are employed in this phase. Building upon the steady solution, the transient-state simulation is carried out utilizing a combination of the mesh motion method and the DDES model. The time step of the transient simulation is 1.39×10^{-4} s, which corresponds to 1° of rotor rotation. The duration of the transient simulation spans 12 complete rotating cycles for both the PJP and DP cases.

C. Numerical validation

In this part, numerical validation is carried out for PJP case with the help of experimental data. The thrust T_r , torque Q_r , and rotation speed n of the rotor are measured by the J25 dynamometer with an uncertainty of 0.2% full scale. The incoming velocity U is measured by the Venturi flow rate with an uncertainty of 0.5% full scale. Figure 4 shows the comparison of experimental and numerical results of hydrodynamic performance curves, including the dimensionless thrust coefficient $K_{Tr} = T_r / \rho n^2 D^4$ and dimensionless torque coefficient $K_{Qr} = Q_r / \rho n^2 D^5$. The K_{Tr} and K_{Qr} obtained from numerical simulations are observed to be lower than the experimental tests, whereas

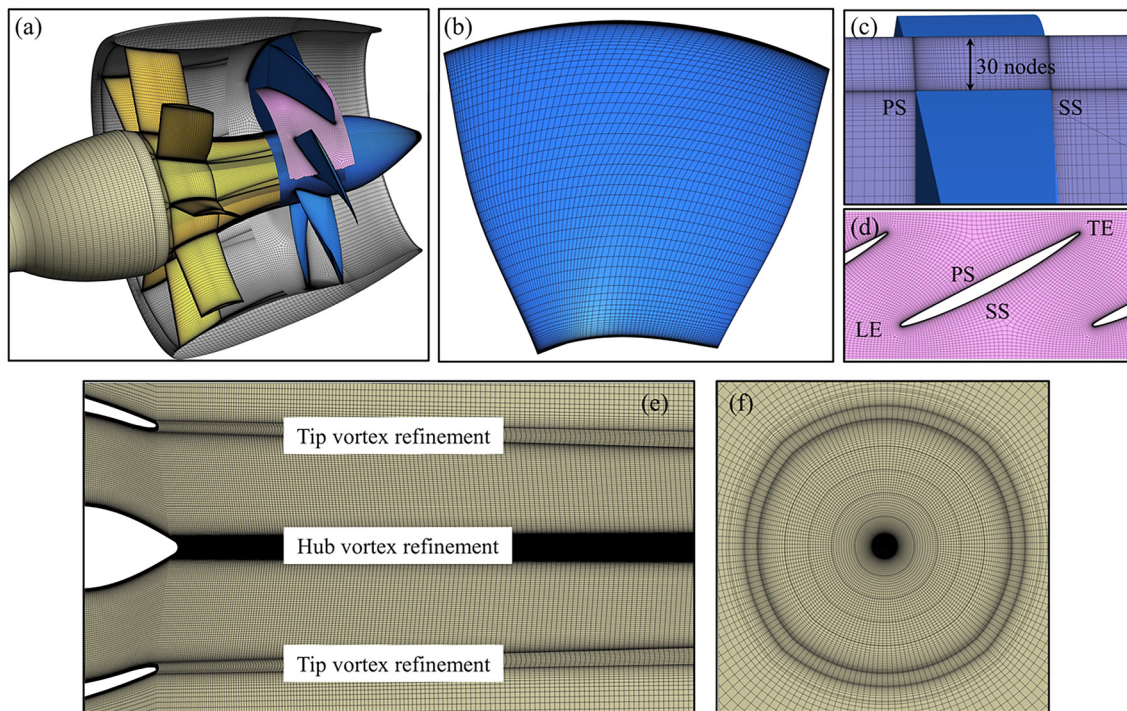


FIG. 3. Computational mesh details of PJP model: (a) global view, (b) single blade, (c) tip clearance, (d) blade passage, and (e) and (f) central-longitudinal plane and transverse plane in the wake field.

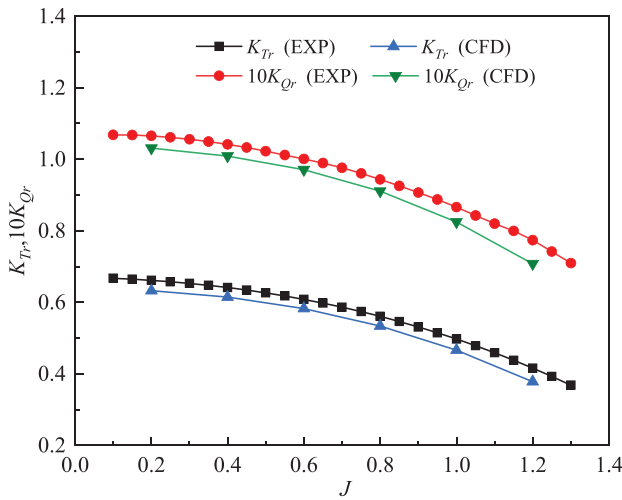


FIG. 4. Hydrodynamic performance curves of PJP.

they show similar trends with operating conditions. The maximum relative errors between experiments and numerical simulations for K_{Tr} and K_{Qr} are found to be 8.1% and 7.5%, respectively. Moreover, the laser doppler velocimetry (LDV) equipment is used to measure the axial velocity in the wake field. The target quarter-circle transversal plane is positioned $0.6D$ away from the duct outlet and has a maximum radius of $0.7D$. This plane contains a total of 80 data points distributed across 5 different angular orientations, as illustrated in Fig. 5(b). Figure 5(a) displays the axial velocity distribution obtained from the numerical simulation for the corresponding region. The numerical simulation results demonstrate a close resemblance to the experimental data in terms of both quantitative and qualitative aspects. Within the region of interest, a high-velocity area ranging from $0.1D$ to $0.4D$ is observed. This high-velocity region also exhibits non-uniformity due to the evolution and interaction of the stator and rotor trailing vortices in the wake field. Both the wake flow and freestream

intersect at approximately $0.4D$. The axial velocity around the center-line region is both lower due to the presence and evolution of the hub vortex. Based on the above analysis, it is believed that the numerical method can be used for wake field investigation and modal analysis for both PJP and DP cases.

III. WAKE FIELD CHARACTERISTICS

A. Flow field analysis

The wake field characteristics of DP and PJP are emphatically analyzed in advance coefficient $J=1.0$ based on the validated numerical simulation method. Figure 6 shows the time-averaged and instantaneous axial velocity field of the DP and PJP models, where the time-averaged field is obtained from 4 rotations of the rotor. The distribution of time-averaged velocity for DP and PJP are to some extent similar. The flow is accelerated through the rotating rotor, and undergoes secondary acceleration under the action of the shrinking duct. The axial velocity is higher than that of the freestream everywhere except in the hub vortex region in both cases. The PJP has a higher axial injection velocity than the DP at the same operating condition, which means that the PJP generates a larger thrust loading according to the momentum theorem. It also reflects the significant influence of the front stator on the performance of the PJP. Figure 6(c) demonstrates a noticeable wake contraction around $1.5D$ in the case of the PJP, whereas this phenomenon is absent in the wake of the DP. The time-averaged axial velocity is also displayed on three transverse planes at $0.7, 1.5,$ and $2.3D$, as shown in Fig. 7. The traces of upstream STV are evident in PJP case, which weaken progressively from $0.7D$ to $2.3D$. Compared with the DP case, the wake field evolution of PJP is considerably more unstable with the modulation of the front stator. In the instantaneous field, the evolving of axial velocity comes with some discontinuities, as affected by the rotor trailing wakes. The rotor trailing vortices interacts with the STV in PJP case, resulting in a higher velocity gradient in localized areas of the wake field.

Figure 8 shows the instantaneous vorticity magnitude and its x -component in entire wake field. The TLV, hub vortex, and thin trailing vortex generated by the rotating rotor blades are found in both DP and

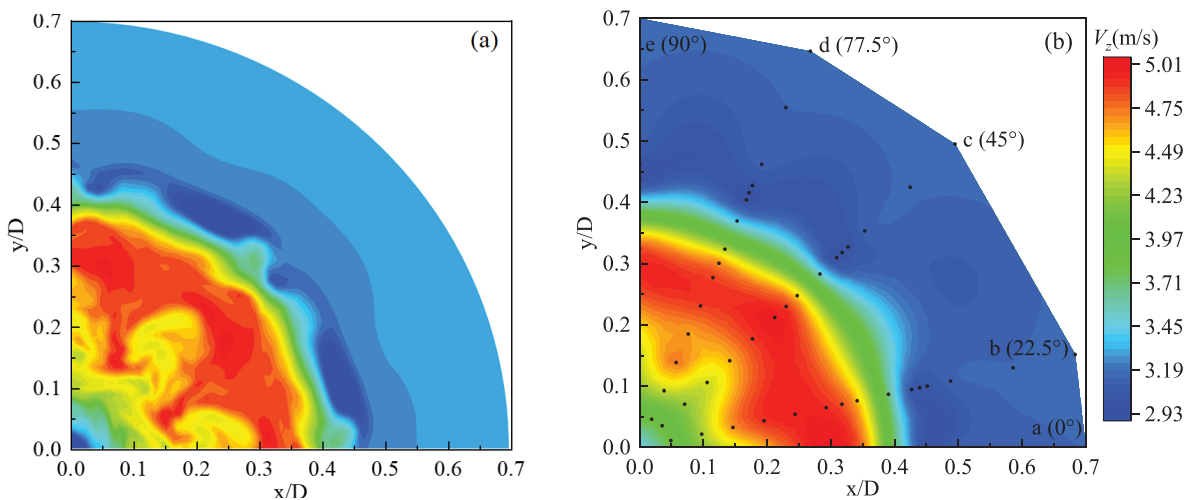


FIG. 5. The axial velocity distribution in the wake field: (a) CFD results. (b) Experimental results.

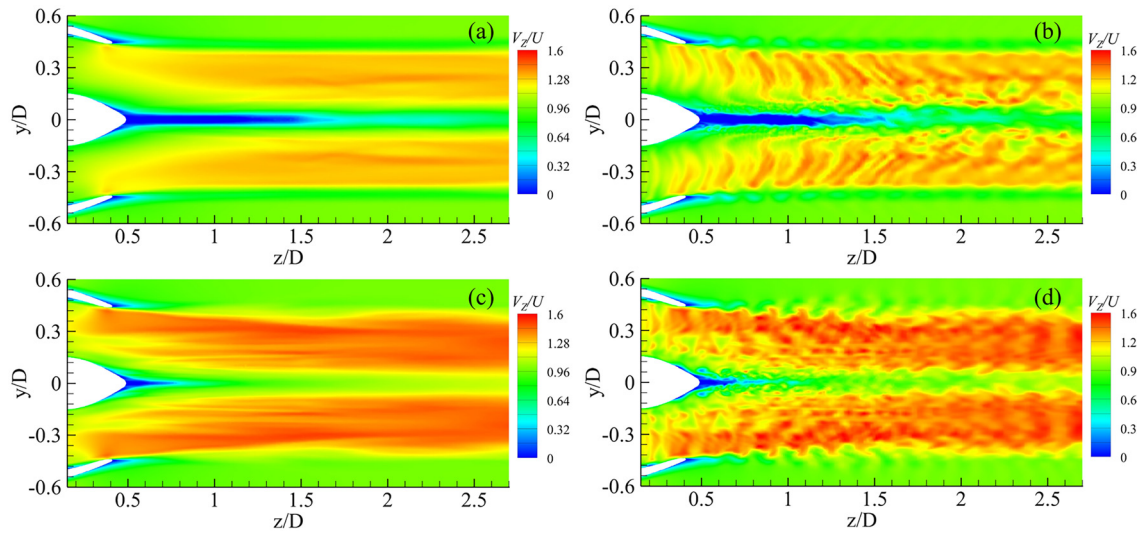


FIG. 6. Time-averaged and instantaneous axial velocity distribution on central-longitudinal plane of DP and PJP wake fields: (a) and (c) time-averaged field for DP and PJP, and (b) and (d) instantaneous field for DP and PJP.

PJP cases, similar to an open propeller.^{1,14} The special DSV which has a opposite sign to the TLV is also found in both two cases, as evident from Figs. 8(b) and 8(d). Moreover, the STV being split into short segments are clearly evident downstream of the rotor in PJP case. The

axial evolution of TLV for two cases are compared from vorticity field. In DP case, the evolution of TLV looks more regular. The TLV leaks from the duct and interacts with the DSV, its vortex core gradually evolves from a circle to an ellipse with progressively weakened intensity

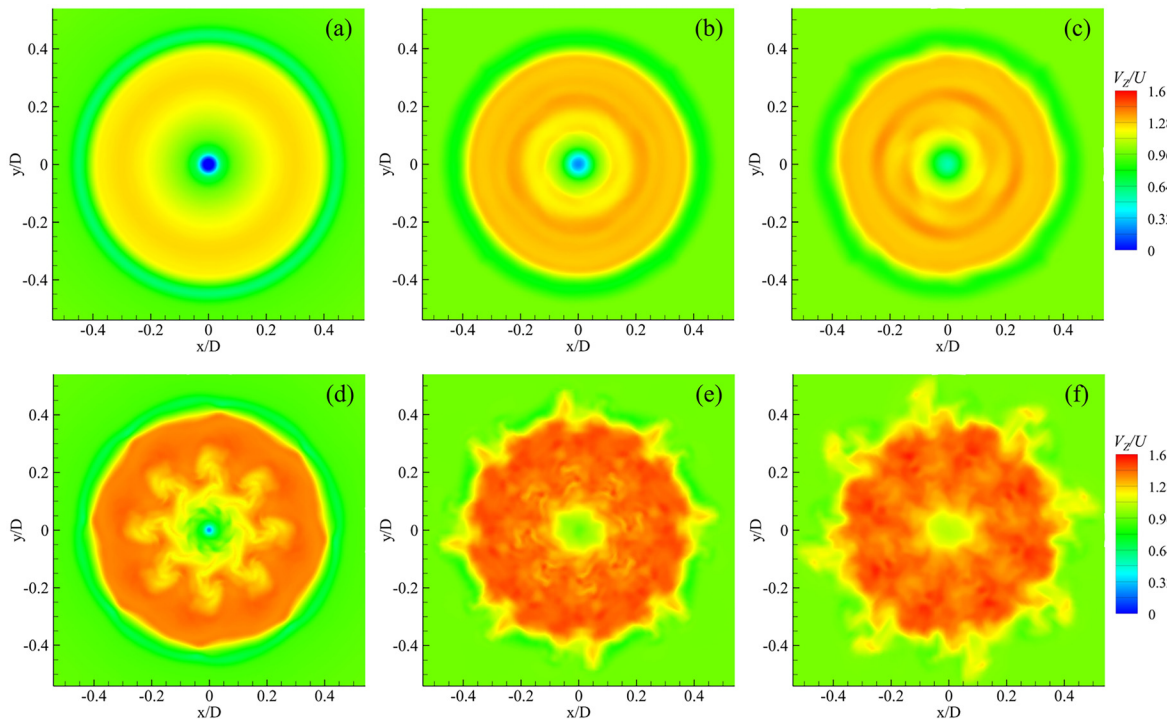


FIG. 7. Time-averaged axial velocity distribution on different transverse planes of DP and PJP wake fields: (a)–(c) 0.7, 1.5, and 2.3D planes of DP; and (d)–(f) 0.7, 1.5, and 2.3D planes of PJP.

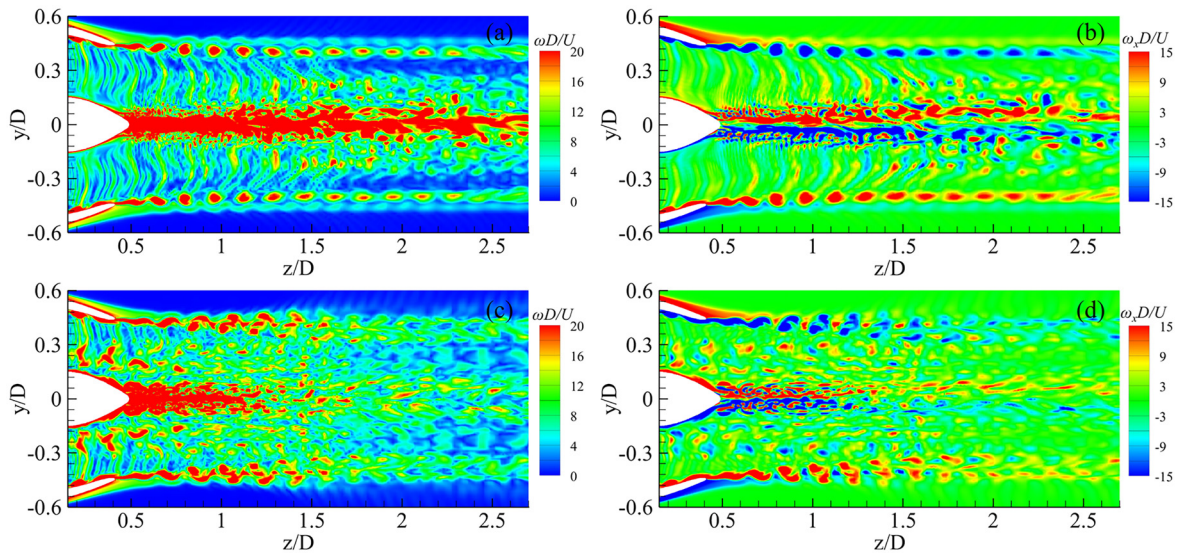


FIG. 8. Instantaneous vorticity and its x-component distribution on central-longitudinal plane of DP and PJP wake fields: (a) and (c) vorticity for DP and PJP, and (b) and (d) x-component vorticity for DP and PJP.

until it is indistinguishable beyond 2.5D. From the perspective of the cross section shown in Fig. 9, it is observed in Fig. 9(a) that the blade trailing vortex undergoes a roll-up process which leads to a gradually bending of its upper part and finally interacts with the adjacent TLV.³⁹

This interaction tends to destabilize the TLV when a rotor with a relatively higher number of blades and weaker tip loading, as Kumar observed in propellers.¹ From 0.7D to 2.3D, the TLV is weakening and the blade trailing vortex gradually breaks up into small vortex

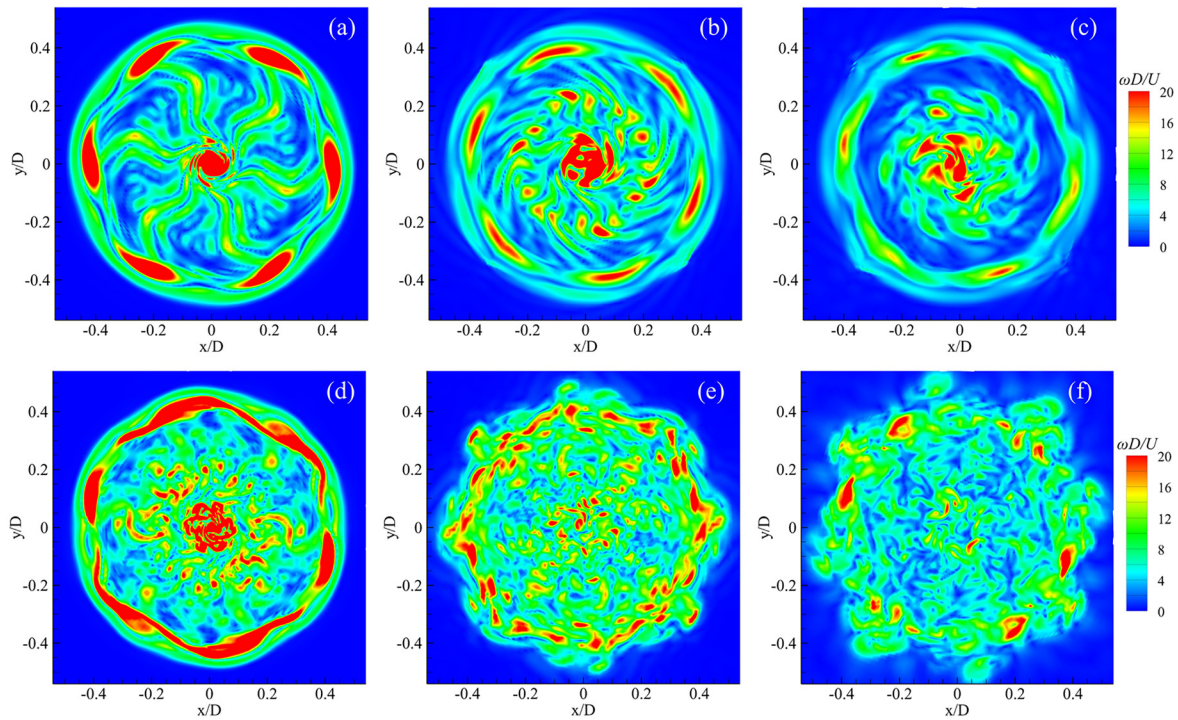


FIG. 9. Instantaneous vorticity distribution on different transverse planes of DP and PJP wake fields: (a)–(c) 0.7, 1.5, and 2.3D planes of DP; and (d)–(f) 0.7, 1.5, and 2.3D planes of PJP.

filaments, so the mutual interaction between them is also decreasing. In PJP case, the TLV quickly induces secondary vortices around 0.9D and then gradually breakdown, eventually undergoes viscous dissipation beyond 1.6D, as evident from Figs. 8(c) and 8(d). From Figs. 9(d)–9(f), it can be seen that the TLV is starting to distort at 0.7D with some oscillations. At 1.5D, the TLV dissolves into some small-scale vortices distributed along a circle and finally it becomes indistinguishable at 2.3D.

The instantaneous axial velocity and vorticity magnitude in the vicinity of the TLV are plotted in Fig. 10 for a cylindrical cut plane at $r/R = 0.84$ to further show the destabilizing evolution of TLV in DP and PJP cases. It can be seen that the TLV is characterized by a low velocity region and a high vorticity region in the axial velocity and vorticity fields, respectively. In DP case, the trajectories of TLVs from different blades are spread in parallel with the similar slope up to 2.5D, as evident from Figs. 10(a) and 10(b). In PJP case, the slope of TLV trajectory decreases abruptly around 1.2D, almost axially, implying that there is not sufficient circumferential velocity to maintain the spiral evolution of the TLV. Moreover, 8 distinct flow traces are visible in Fig. 10(c), which has the same number with front stator blades. To further explain the difference of TLV trajectories in DP and PJP cases, the

time-averaged circumferential velocities of the three transverse planes are shown in Fig. 11. The circumferential velocity in the DP case is typically characterized by a negative sign and reaches its maximum value in the hub vortex region, and its intensity is decreasing along the axial direction. Obviously, the circumferential velocity in the wake field of DP is generated by the rotating rotor, so that has a same sign with the rotor rotating direction. However, the circumferential velocity in the PJP case has a opposite sign compared to the DP case. In PJP design, the front stator is designed to generate an appropriate negative pre-swirl flow upstream of the rotor, which is expected to neutralize the circumferential velocity generated by the rotating rotor to absorb tangential energy. In our PJP case, the pre-swirl effect is not completely offset in the wake field due to the imperfect design of the stator geometry, so the circumferential velocity has a positive sign. In short, the negative pre-swirl effects of stator lead to the weakening of the spiral evolution of the TLV in the PJP case. Back to Fig. 10, it is observed from the vorticity field of PJP that several secondary vortices are induced on each TLV, splitting the TLV into short segments with the similar length, thus disrupting the continuity of the TLV spirals. The uniform incoming flow is divided by the front stator blades into 8 circumferentially distributed flow channels when it is entering the duct,

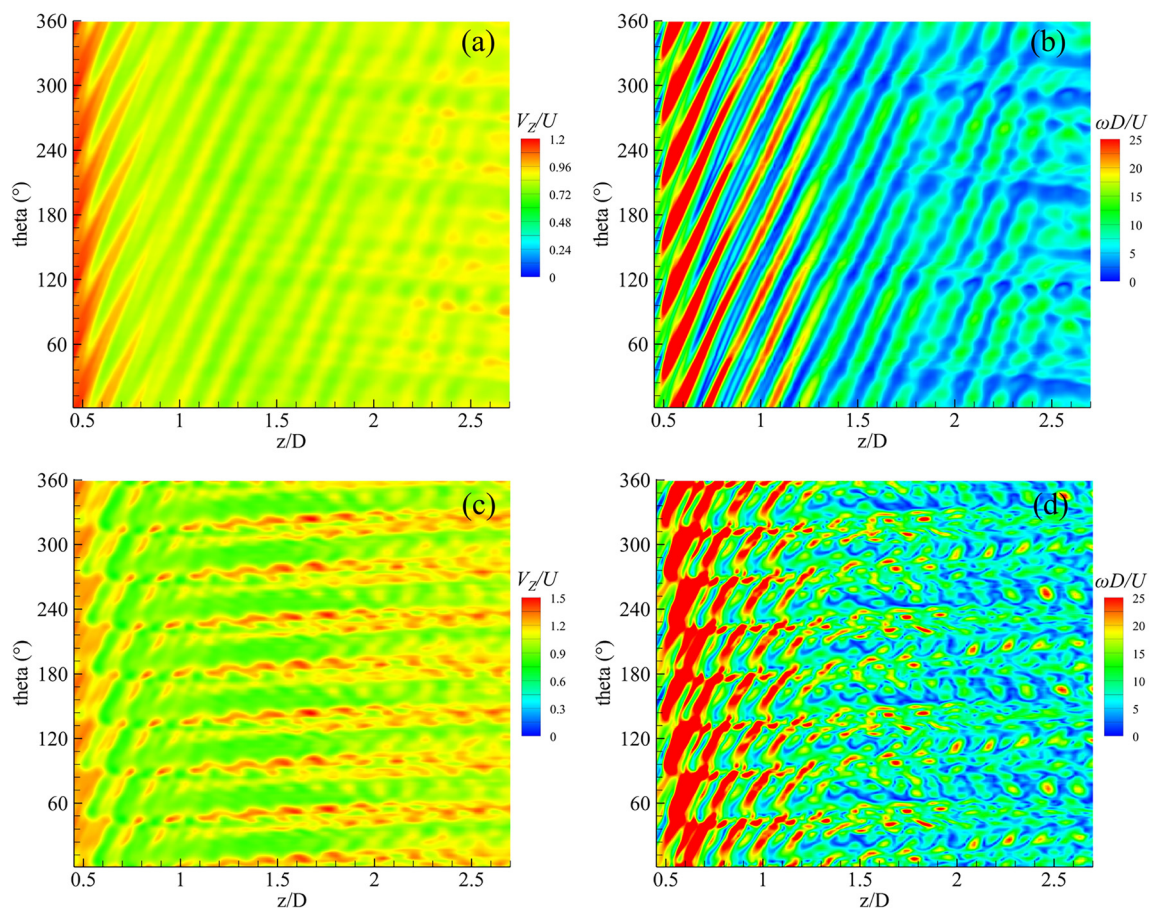


FIG. 10. Instantaneous axial velocity and vorticity distribution on the cylindrical cut plane at $r/R = 0.84$ for DP and PJP cases: (a) and (c) axial velocity for DP and PJP, and (b) and (d) vorticity for DP and PJP.

05 April 2024 07:28:53

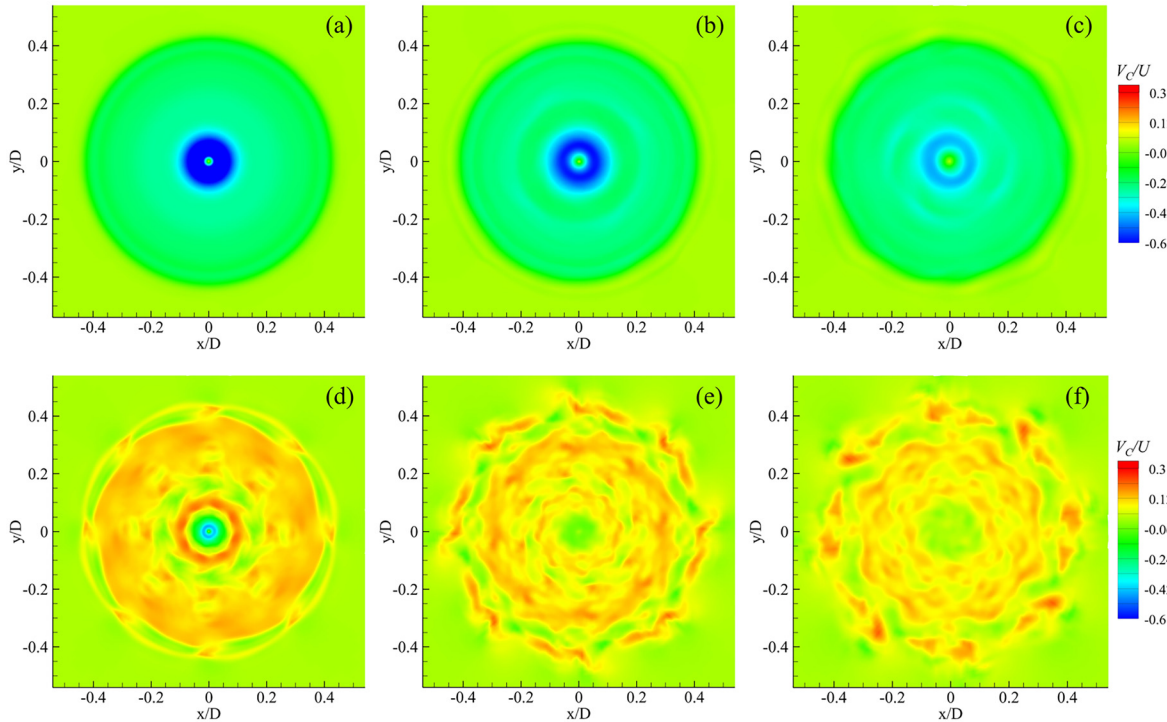


FIG. 11. Instantaneous circumferential velocity distribution on different transverse planes of DP and PJP wake fields: (a)–(c) 0.7, 1.5, and 2.3D planes of DP; and (d)–(f) 0.7, 1.5, and 2.3D planes of PJP.

the traces of flow channels splitting are still evident in the wake field, thus inducing secondary vortices of the TLV, this is also noticed by Qin *et al.*³⁹ For the hub vortex, it quickly destabilizes and breaks down in PJP case owing to the more considerable perturbations from the upstream stator trailing vortices. In the DP case, the hub vortex maintains the streamwise evolution for a longer distance and has a decreasing swirl velocity with increasing distance from the rotor, as evident from Figs. 6, 8, and 11.

To know the energy distribution in the wake field, the kinetic energy, $KE = 0.5(V_x^2 + V_y^2 + V_z^2)$ and turbulence kinetic energy, $TKE = 0.5(V_x'^2 + V_y'^2 + V_z'^2)$ for two cases are shown in axial and transverse planes, respectively, as shown in Figs. 12–14. The KE describes the energy transfer between the propeller and the fluid, and the TKE is related to flow instability and turbulence generation.²⁴ As shown in Fig. 12, the KE distribution in the wake field of DP and PJP is discontinuous, consistent with the features of the axial velocity in Fig. 6. The KE in the wake field of PJP is higher than in that of DP, and is mainly concentrated in the upper part of the slipstream. This further indicates that the existence of the front stator is important for improving the energy conversion between the rotating rotor and the fluid in such propulsors. From the perspective of the transverse sections shown in Fig. 13, it is observed that the magnitude of KE increases and then decreases from 0.7D to 2.3D in both cases. The evolution of the STV brings a large kinetic energy gradient in the wake field of PJP, thus resulting in a more chaotic kinetic energy field. In the TKE field, it is evident that higher TKE values are concentrated in the regions of the TLV and hub vortex in both the DP and PJP cases. In

the TLV region, the highest TKE values are observed near the outlet of the duct. This is primarily due to the interaction between the DSV and the TLV, which leads to the increased turbulence. As we move axially downstream in the TLV, the TKE is progressively decreasing in both cases, which is consistent with the understanding that turbulence tends to dissipate and decrease as it travels downstream. Based on the previous analysis for vorticity fields, it is known that the TLV of PJP is more unstable, so it generates a higher TKE than DP. On the other hand, the hub vortex of DP appears to be stronger, hence resulting in a higher turbulence level and with it more TKE than PJP.

B. Vortex structures

In this part, coherent vortical structures in the wake of DP and PJP are visualized based on the omega vortex identification method developed by Liu *et al.*⁴⁰ In this method, the vorticity is decomposed into vortical vorticity and non-vortical vorticity. A dimensionless parameter Ω is introduced to identify the vortex, which refers to the percentage of vortical vorticity to the overall vorticity for a vortex structure, as shown in the following equation:

$$\Omega = \frac{b}{a + b + \epsilon}, \tag{6}$$

where a and b are the square of Frobenius norm of A and B , they are $a = \|A\|_F^2$ and $b = \|B\|_F^2$. A and B are the symmetric and antisymmetric parts of the velocity gradient tensor ∇V , which is, respectively, expressed as

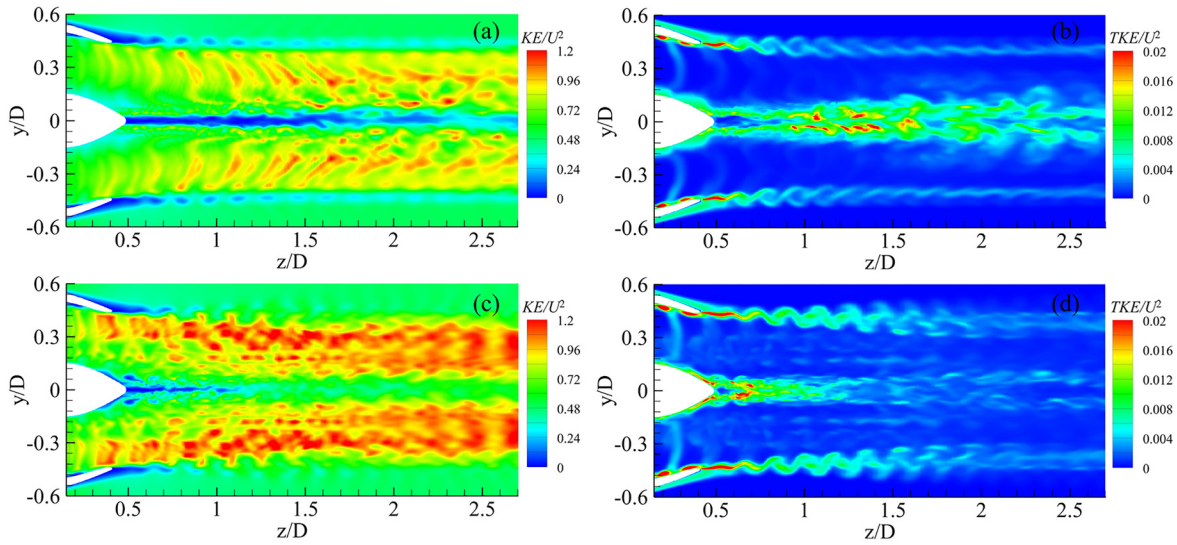


FIG. 12. Instantaneous KE and TKE distribution on central-longitudinal plane of DP and PJP wake fields: (a) and (b) KE and TKE for DP case, and (c) and (d) KE and TKE for PJP case.

$$A = \frac{1}{2}(\nabla V + \nabla V^T), \quad B = \frac{1}{2}(\nabla V - \nabla V^T). \quad (7)$$

A small positive parameter ε is included in the denominator of Eq. (6) to avoid nonphysical noises, it is empirically determined as

$\varepsilon = 0.001 \times (b - a)_{\max}^{.41}$. In this study, the vortex structures are visualized by the iso-surface with a threshold $\Omega = 0.52$.

As depicted in Fig. 15, the wake vortex structures of DP and PJP models are well visualized, both including the TLV, the DSV and the

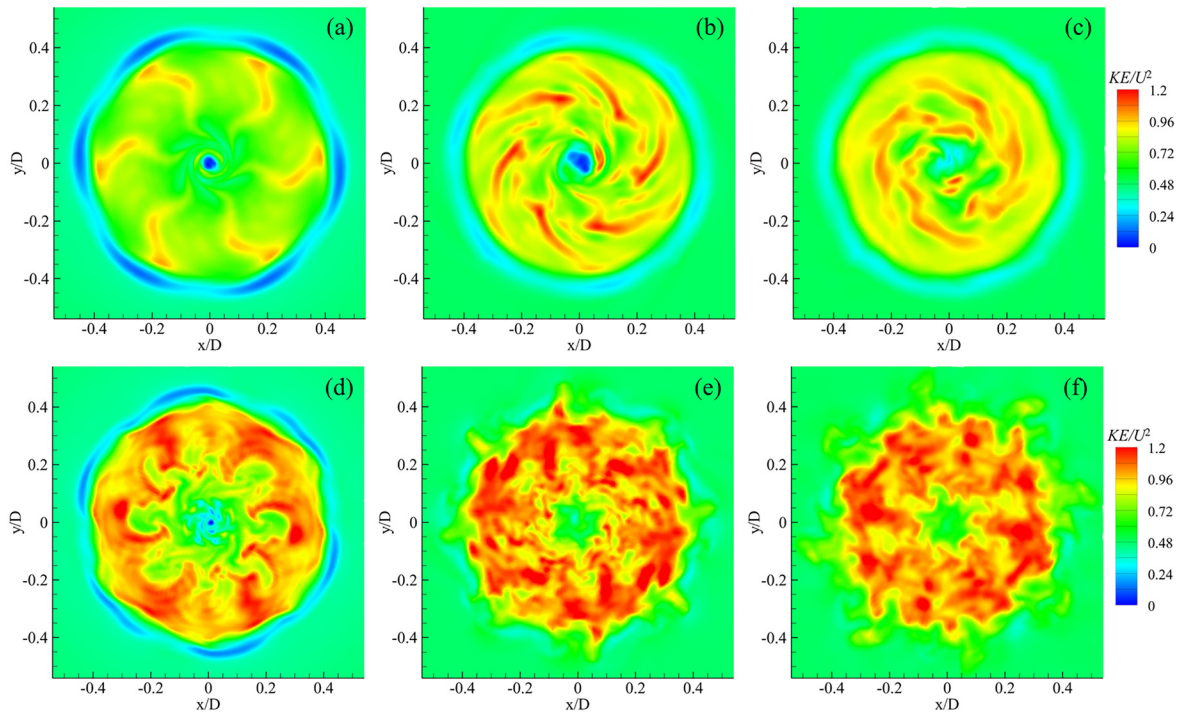


FIG. 13. Instantaneous KE distribution on different transverse planes of DP and PJP wake fields: (a)–(c) 0.7, 1.5, and 2.3D planes of DP; and (d)–(f) 0.7, 1.5, and 2.3D planes of PJP.

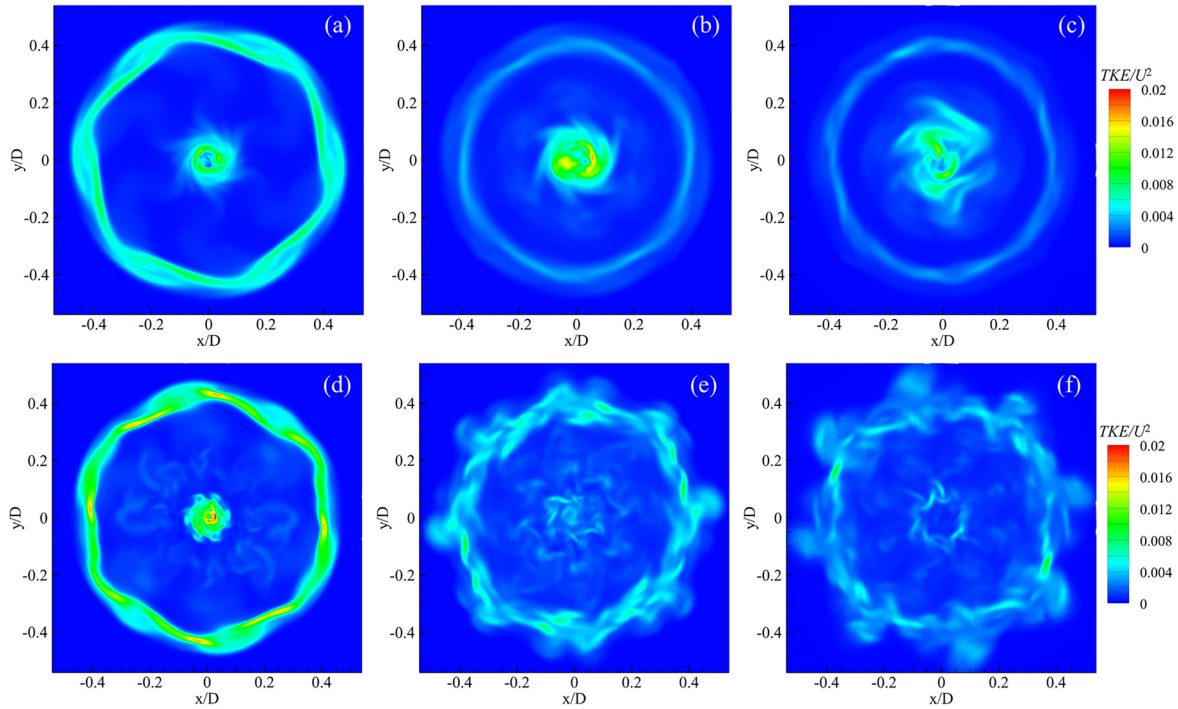


FIG. 14. Instantaneous TKE distribution on different transverse planes of DP and PJP wake fields: (a)–(c) 0.7, 1.5, and 2.3D planes of DP; and (d)–(f) 0.7, 1.5, and 2.3D planes of PJP.

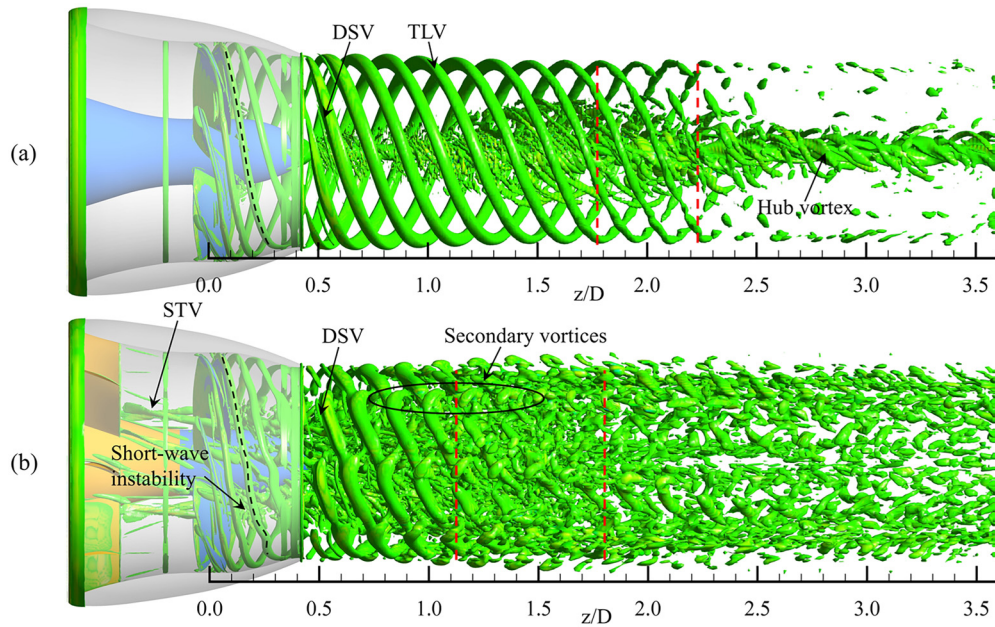


FIG. 15. Wake vortex structures of DP and PJP: (a) DP and (b) PJP.

05 April 2024 07:28:53

hub vortex. Specifically, the PJP also contains the STV, which is cutoff by the rotor, generating numerous small-scale vortex structures downstream of the rotor. In the DP case, the TLV leaks out from the rotor suction surface under the action of pressure difference and spirally develops downstream with a progressive decrease in strength. Its entire evolution is divided into three stages, namely, the stabilization stage (before 1.8D), the TLV maintains a continuous spiral shape; the transition stage (1.8D–2.2D), the TLV is starting to get unstable with a gradual disruption of the spiral trajectory; and the breakdown stage (after 2.2D), the TLV is completely broken down into numerous small-scale vortex structures. These stages represent the different phases of the TLV’s development and behavior, as characterized by the red dashed lines in Fig. 15. In consistent with the previous flow field results, the hub vortex is present throughout the wake field and develops in a twisted manner. In the PJP case, the TLV shows short-wave instability with sinusoidal wave before it leaves the duct, which is caused by periodic fluctuation in incidence angle due to modulation of front stator to the rotor incoming flow.³⁹ The secondary vortices are gradually forming and escaping from the TLV, thus destabilizing the TLV. The evolutionary stage of TLV is considerably different from that in DP, which are the stabilization stage (before 1.1D), the transition stage (1.1D–1.8D) and the breakdown stage (after 1.8D).

Combined with the flow field analysis in Sec. III A, the differences between the wake vortex dynamics of DP and PJP are summarized in three aspects. First, the front stator of the PJP induces the STV, which interacts with the rotor trailing vortices as well as the hub vortex, deteriorating the stability of its wake field. Second, the segmentation effect of the front stator on the flow domain triggers the generation of secondary vortices of TLV and accelerates its destabilization. Finally, the negative pre-swirl of the front stator largely absorbs the circumferential velocity in the wake field and moderates the spiral behavior of the TLV.

IV. DYNAMIC MODE DECOMPOSITION ANALYSIS

A. Theory

The DMD is widely used in fluid dynamics community as a method to decompose complex flows into a simple representation based on spatiotemporal coherent structures. Schmid *et al.*^{30,31} first developed the DMD algorithm and demonstrated its ability in flow field analysis. In this study, the standard DMD algorithm is employed and its mathematical principle is briefly introduced.

As DMD is a data-driven analysis method, the modal information is derived from time-resolved snapshots, the matrix used to collect the flow data are expressed as

$$\mathbf{V}_1^N = [\mathbf{v}_1, \mathbf{v}_2, \mathbf{v}_3, \dots, \mathbf{v}_i, \dots, \mathbf{v}_N], \quad (8)$$

where \mathbf{v}_i is the i th instantaneous snapshot contains M spatial points, and N is the total number of snapshots. DMD assumes there is a constant linear mapping \mathbf{A} connecting the flow field \mathbf{v}_i to the next \mathbf{v}_{i+1} ,

$$\mathbf{v}_{i+1} = \mathbf{A}\mathbf{v}_i. \quad (9)$$

The snapshot matrix \mathbf{V}_1^N can be written as a Krylov sequence,

$$\mathbf{V}_1^N = [\mathbf{v}_1, \mathbf{A}\mathbf{v}_1, \dots, \mathbf{A}^{N-1}\mathbf{v}_1]. \quad (10)$$

It is assumed that \mathbf{v}_N can be expressed as a linear combination of the previous $N-1$ snapshots,

$$\mathbf{v}_N = c_1\mathbf{v}_1 + c_2\mathbf{v}_2 + \dots + c_{N-1}\mathbf{v}_{N-1} + \mathbf{r}, \quad (11)$$

where c_i are the polynomial coefficient and \mathbf{r} is the residual vector. By combining Eqs. (10) and (11), it can be derived,

$$\mathbf{A}\mathbf{V}_1^{N-1} = \mathbf{V}_2^N = \mathbf{V}_1^{N-1}\mathbf{S} + \mathbf{r}\mathbf{e}_{N-1}^T, \quad (12)$$

where \mathbf{e}_{N-1} denotes the $(N-1)$ th unit vector, and the companion matrix \mathbf{S} is described as

$$\mathbf{S} = \begin{bmatrix} 0 & & & c_1 \\ 1 & 0 & & c_2 \\ & \ddots & \ddots & \vdots \\ & & 1 & 0 \\ & & & c_{N-2} \\ & & & 1 & c_{N-1} \end{bmatrix}. \quad (13)$$

To compute the matrix \mathbf{S} , the singular value decomposition (SVD) is commonly used for \mathbf{V}_1^{N-1} , that is, $\mathbf{V}_1^{N-1} = \mathbf{U}\mathbf{\Sigma}\mathbf{W}^H$. Based on similarity transformation, the approximate matrix $\tilde{\mathbf{S}} = \mathbf{U}^H\mathbf{V}_2^N\mathbf{W}\mathbf{\Sigma}^{-1}$, where \mathbf{U}^H is a complex conjugate transpose of \mathbf{U} . By calculating the eigenvector \mathbf{y}_i and corresponding eigenvalue λ_i of $\tilde{\mathbf{S}}$, the DMD modes can be obtained,

$$\phi_i = \mathbf{U}\mathbf{y}_i. \quad (14)$$

The different DMD modes are able to capture the spatial structure and temporal evolution of the propeller wake flow, and the modal energy criterion defined by Eq. (15) is employed to select representative modes with higher modal energy,³⁵

$$\|\phi_i\| = \frac{1}{\|\mathbf{W}^H\mathbf{\Sigma}^{-1}\mathbf{y}_i\|}. \quad (15)$$

The modal growth rate g_i and modal frequency f_i can also be obtained from the real part and imaginary part of the eigenvalue λ_i , respectively, as shown in the following equation:

$$\begin{aligned} g_i &= \text{Re}(\ln(\lambda_i)/\Delta t), \\ f_i &= \text{Im}(\ln(\lambda_i)/\Delta t)/2\pi. \end{aligned} \quad (16)$$

B. Dataset collection

The DMD technique is used to further investigate the coherent structure in the DP and PJP wake fields. Shi *et al.*^{24,25} demonstrated that the modes derived from the vorticity magnitude are capable of capturing detailed wake vortex structures and their instabilities. Therefore, the vorticity is also selected as the variable for modal decomposition in this study. The modal analysis is carried out on one central-longitudinal plane and three transverse planes (located at 0.7D, 1.5D, and 2.3D) used in Sec. III A.

They contain 74 027, 26 375, 25 110, and 24 997 spatial data points at an instant, respectively. In temporal dimension, datasets with a sampling time interval $\Delta t = 2.78 \times 10^{-4}$ s (2° of rotor rotation) and a sampling duration of 4 rotor revolutions are collected, with 720 snapshots in each case. The resultant sampling frequency satisfies the Nyquist–Shannon criterion.^{42,43} The modal analysis results for different planes are presented, respectively, in Secs. IV C 1 and IV C 2.

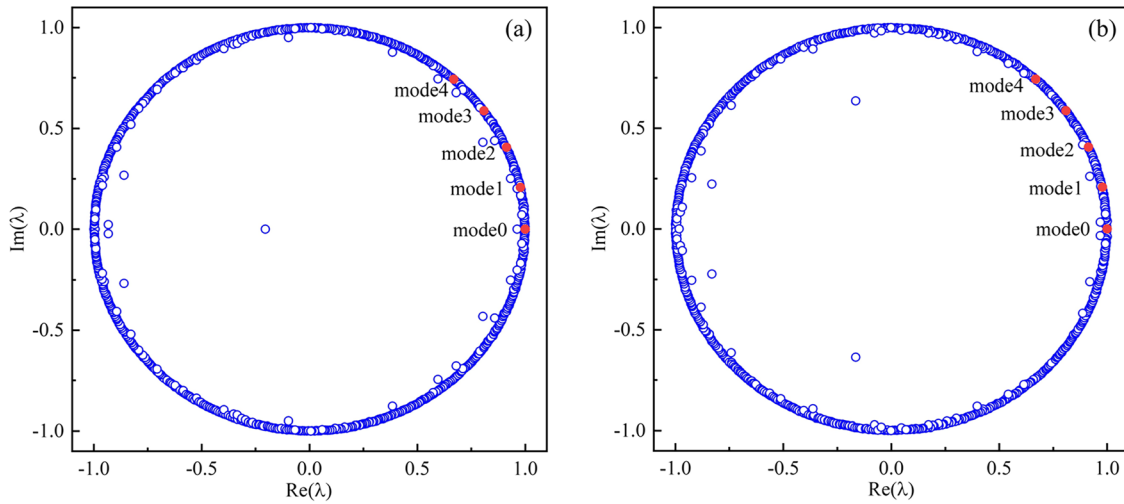


FIG. 16. Distribution of DMD eigenvalues on central longitudinal plane of DP and PJP wake fields: (a) DP and (b) PJP.

C. Modal analysis results

1. Central-longitudinal plane

The modal analysis is first carried out in the central-longitudinal plane to investigate the axial evolution of the wake coherent structures in both DP and PJP cases. Figure 16 presents the eigenvalues of various orders of DMD modes on the complex plane for both cases. The horizontal scale denotes the real part of the eigenvalue and the vertical scale denotes its imaginary part. It can be seen in both cases that most of the eigenvalues lie on the unit circle, corresponding to stable or periodic modes. A few eigenvalues lie within the unit circle, corresponding to convergence modes. This reflects that the modal decomposition has favorable convergence based on the constructed snapshot dataset, and the wake flow in DP and PJP is both dominated by the periodic flow structures.^{32,34}

To identify the modes contributing prominently to wake dynamics of DP and PJP, the modal energy criterion defined in Eq. (15) is

used to illustrate the energy spectrum of different modes, as shown in Fig. 17. The horizontal axis is dimensionless with the blade pass frequency $f_{BPF} = 120$ Hz and the energy spectrum is shown in the frequency range of the first $8f_{BPF}$ with relatively higher energy. The mode with $\kappa = 0$ exhibits the highest energy, while the other dominant modes are located at the f_{BPF} and its integer multiples. The modal analysis primarily focuses on the first five modes with the highest energy, which are named as mode 0–4, respectively. In Fig. 17, the modal energy spectrum magnitude of the PJP wake field is found to be larger than that of the DP wake field overall, which indicates that the PJP wake field exhibits more complicated turbulent coherence structures. In particular, the energy level of the modes in the PJP wake field is not exactly decreasing with frequency as in DP. The energy level of mode 4 is higher than that of mode 3. As we know that the wake field characteristics of PJP are commonly modulated by the stator and rotor, the number of rotor and stator blades in this study is not mutually prime

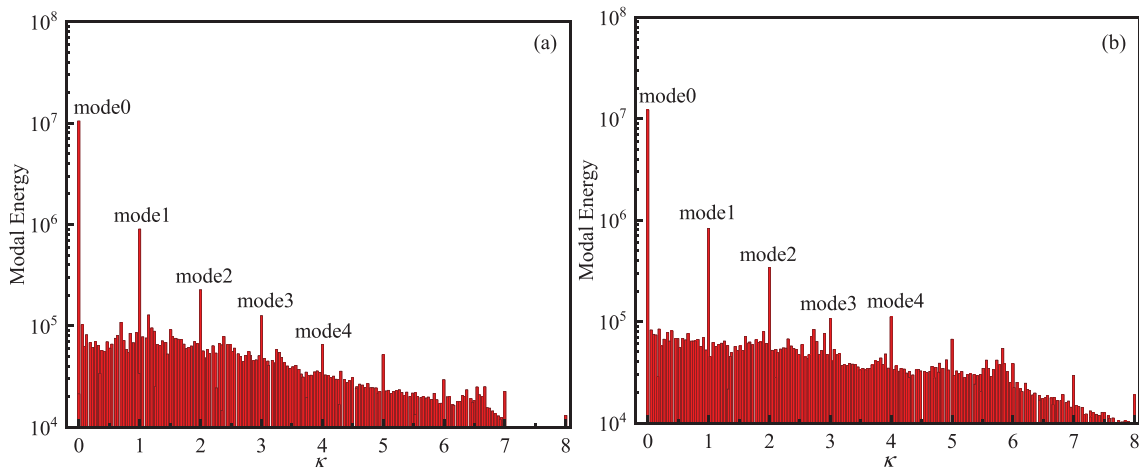


FIG. 17. Energy spectrum on central-longitudinal plane of DP and PJP wake fields: (a) DP case and (b) PJP case.

05 April 2024 07:28:53

leading to rotor–stator resonance, which increases the energy value of at $\kappa = 4$ and its multiples. This will further increase the excitation force of the propulsion system and should be avoided in the design.^{7,9}

Figure 18 shows the coherent flow structures in the wake field of DP and PJP corresponding to modes 0–4. The mode 0 with zero frequency represents the time-averaging vorticity field. The high vorticity is primarily located in the hub vortex and TLV regions. There is also a clear vorticity downstream of the rotor in PJP generated by the

evolution of the STV. Comparing the DP and PJP cases, it can be observed that the hub vortex in DP is stronger than that in PJP, and the TLV in PJP looks more unstable than that in DP, which is consistent with the instantaneous vorticity field shown in Fig. 8.

Figures 18(b) and 18(g) present the mode 1 for both DP and PJP wake field. In DP case, the evolution of TLV is characterized by the modal structures with alternating positive and negative values. It can be clearly seen that the TLV is leaking from the duct and its topological

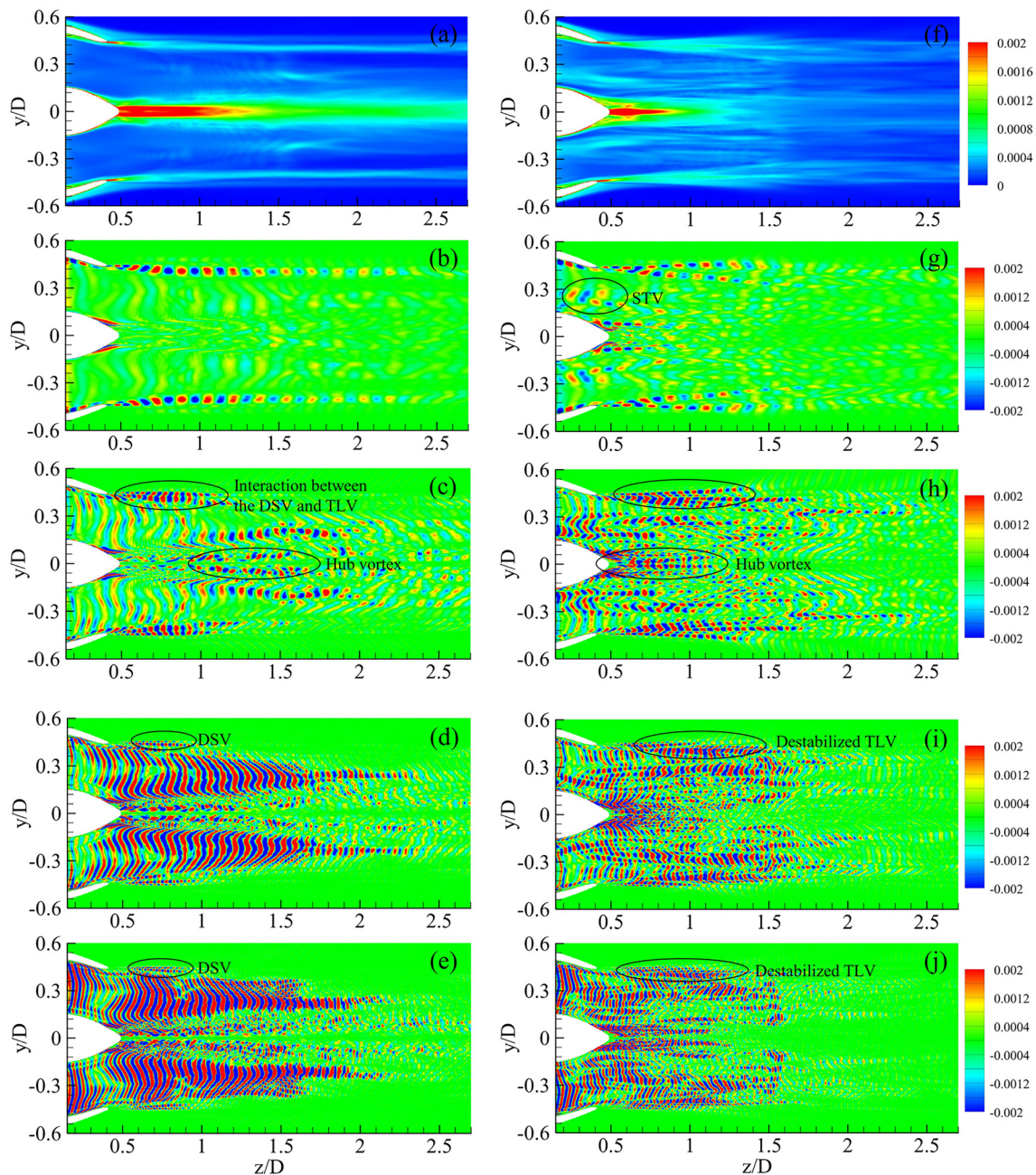


FIG. 18. DMD modes on central-longitudinal plane of DP and PJP wake fields: (a)–(e) modes 0–4 of DP, and (f)–(j) modes 0–4 of PJP.

05 April 2024 07:28:53

structure is relatively stable with a gradual decrease in intensity. In PJP case, the TLV quickly splits into two parts after shedding from the duct due to the generation of the secondary vortex structures. This mode also highlights the evolution of STV downstream the rotor in PJP, as evident from the small-scale modal structures behind the rotor and near the hub.

The mutual interaction process between the DSV and TLV in the near wake field can be clearly identified by mode 2 in both cases, as shown in Figs. 18(c) and 18(h). It is evident that the shedding DSV is merged with the TLV between 0.5 and 1.0D in DP case, as marked by the black ellipse. In PJP case, the breakdown of the TLV coherent structure is clearly shown, forming many small-scale vortex filaments that evolve downstream in a triangular diffusion pattern. In addition, the features of the hub vortex in both cases are also reflected by this mode. The higher TKE region around the hub vortex in DP (about 1–1.7D) and PJP (about 0.5–1.1D) shown in Fig. 12 is highly correlated with the modal structures of hub vortex indicated by mode 2. This further suggests that mode 2 can represent the highly turbulent region of the hub vortex. Modes 3 and 4 are largely correlated with the axial evolution of the rotor trailing vortices in DP and PJP cases. As shown in Figs. 18(d) and 18(e), the blade trailing vortex sheds from the trailing edge of rotor due to the spanwise variation of the blade circulation, and it gradually weakens in the far wake field with viscous dissipation.¹ In PJP case, the spatial scale of the rotor wake represented by modes 3 and 4 is smaller than in DP, and this modal feature is indistinguishable beyond 1.6D, as shown in Figs. 18(i) and 18(j). The mutual interaction between the small-scale vortex filaments of STV and the rotor blade trailing vortex leads to the rapid disintegration of the rotor wake in PJP case. Moreover, it is observed that the modal structure of DSV is still evident in the modes 3 and 4 of DP case, and the decomposing small-scale TLV structures are visible in the modes 3 and 4 of PJP case.

2. Transverse planes

The modal analysis is also carried out on three different transverse planes along the axial direction. From the vortex topologies shown in Fig. 15, it can be seen that these three planes are, respectively, located in the stable, transition and breakdown regions of the PJP

wake field, so they can be representatively compared with the DP wake field to know the evolution mechanism differences between them.

Figures 19–21 illustrate the modal energy spectra of the three planes in DP and PJP cases. It is observed that the energy level progressively decreases streamwise in both cases, and decreases more rapidly in PJP. In Fig. 19, the overall magnitude of the energy spectrum covering the $8f_{BPF}$ frequency range in PJP is higher than in DP at 0.7D. However, the energy spectrum value of PJP decreases remarkably at 1.5D and similarly at 2.3D, as evident from Figs. 20(b) and 21(b). This indicates that the PJP wake field with more complex coherent structures under the co-modulated of the stator and rotor. Consequently, the mutual interaction of different scale vortex structures will also be stronger, thus triggering the instability of the wake vortex system earlier and causing a faster dissipation of its modal energy. Comparing the energy spectra of DP and PJP, it can be found that the energy spectrum characteristics of PJP are mainly dominated by the f_{BPF} and its multiples in three transverse planes. However, the energy spectrum features are not completely dominated by the f_{BPF} and its multiples in DP case. It can be seen from Fig. 19(a) that a mode with the second highest energy appears at $f = 283.7$ Hz, which dominant in the modal structure of this plane. This special mode is labeled as mode A. Furthermore, the same observation is found in the 1.5D plane, as shown in Fig. 20(a), where there are two modes with higher modal energy located at $f = 58$ Hz and $f = 195$ Hz, labeling them as mode B and mode C, respectively. In Fig. 21(a), it is found that the flow structure in this plane is mainly characterized by the averaged vorticity field represented by the zero frequency. The second highest energy mode is labeled as mode D. These four special modes will be analyzed later via the modal structures to understand their origination. From the analysis of energy spectrum in different transverse planes, it is concluded that the streamwise evolution pattern of PJP wake structures is completely different from that of DP.

To further understand the flow details of the wake field at different evolution stages in DP and PJP cases, the modal structures located at $\kappa = 1$ to $\kappa = 4$ are visualized in three transverse planes, and these four modes are also named as modes 1–4, as shown in Figs. 22–24. In the DP case, the mode 1 characterizes the main TLV structures and the rotor trailing vortices, it can be clearly seen from Fig. 22(a) that six

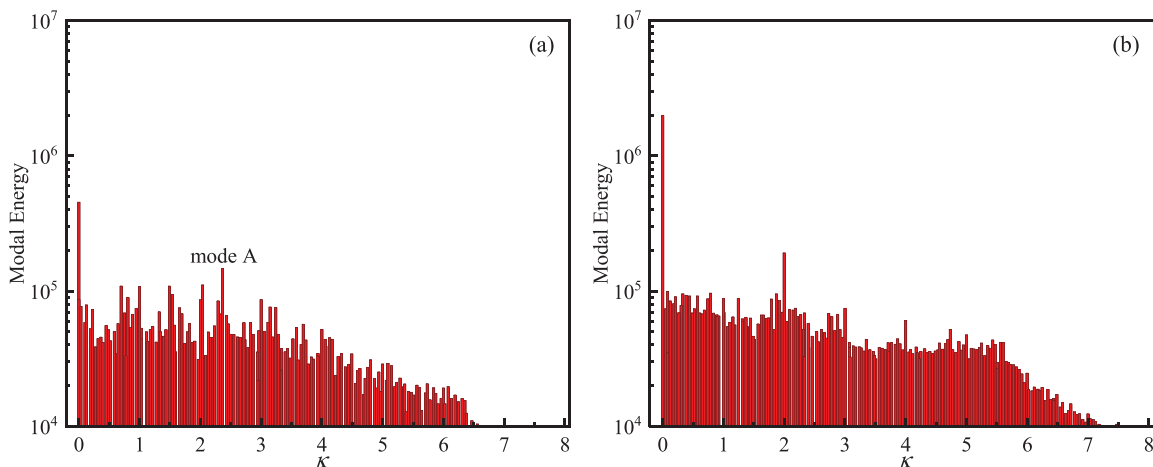


FIG. 19. Energy spectra on 0.7D transverse plane of DP and PJP wake fields: (a) DP case and (b) PJP case.

05 April 2024 07:28:53

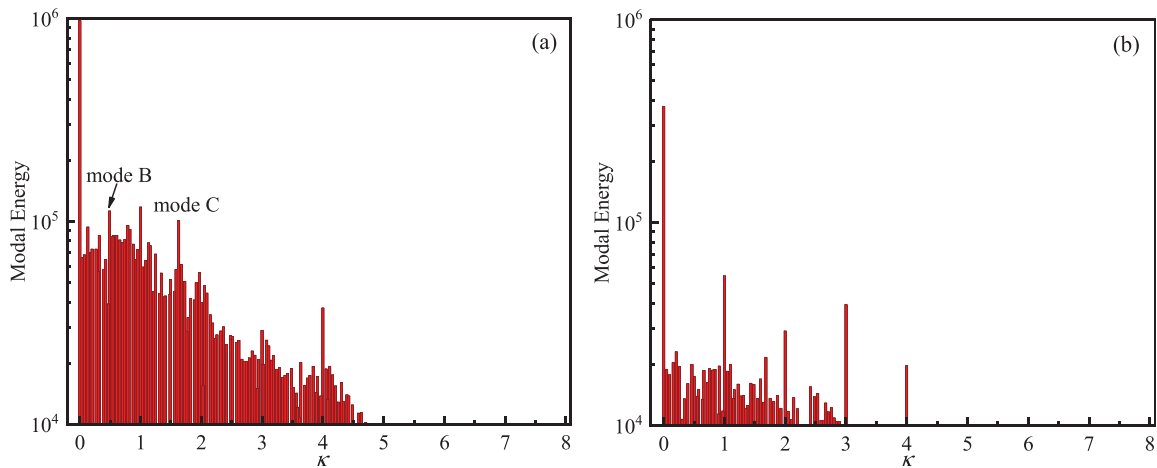


FIG. 20. Energy spectra on 1.5D transverse plane of DP and PJP wake fields: (a) DP case and (b) PJP case.

pairs of modal structures with alternating positive and negative values appear in the rotor wake core region and the TLV developing region, respectively. The mode 2 identifies the mutual interaction between the rotor trailing vortices and the adjacent TLV, and also interaction between the TLV and the DSV. It is clearly seen in Fig. 22(b) that two layers of modal structures are distributed along the circumferential direction with a slight phase difference. The outer layer with lower intensity represents DSV, and the inner layer with higher intensity denotes TLV. They are fused together but not changing the topology of each one. Moreover, the roll-up process of the rotor trailing vortices can also be clearly seen. The upper part of the rotor trailing vortices is in contact with the inner side of the TLV. The modes 3 and 4 mainly reflect the axial evolution of the rotor trailing vortices, and the modal structures of DSV and TLV are still visible. Figures 22(e)–22(h) show the different orders of modes at 0.7D plane in PJP case. In mode 1, the TLV appears more turbulent than in DP, and the STV is apparent in this mode, while the rotor trailing vortices are completely disrupted and poorly distinguished. In mode 2, the interaction between the TLV

and DSV looks stronger and more disordered. The more chaotic rotor wakes are presented by modes 3 and 4, and the disordered mutual interaction between the rotor trailing vortices and the TLV can be identified by these two higher order modes instead of mode 2.

In Fig. 23, the TLV of DP still remains stable as seen from mode 1, while the rotor trailing vortices undergo circumferential and radial diffusion accompanied by a more chaotic turbulent structure of various scales, as evident from Fig. 23(a). In mode 2, the TLV and DSV are no longer interacting with each other as their intensities decrease. For PJP case, the wake coherent structures are in the transition stage from stable to complete disintegration, the wake field is completely chaotic and loses its stability in this plane, the TLV and rotor trailing vortices are mixed together and indistinguishable in all the four different modes. At 2.3D plane shown in Fig. 24, the TLV of DP shows significant circumferential diffusion with more unstable modal structures, as seen from mode 1. Compared to the flow field at 0.7 and 1.5D planes, the viscous dissipation process of the rotor trailing vortices in DP case can be clearly identified by the mode 4. The wake structures

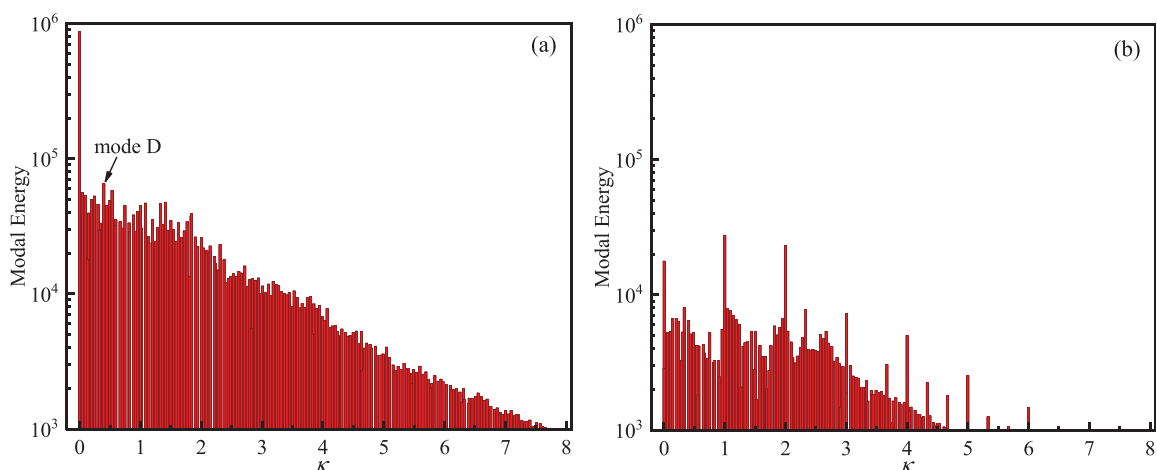


FIG. 21. Energy spectra on 2.3D transverse plane of DP and PJP wake fields: (a) DP case and (b) PJP case.

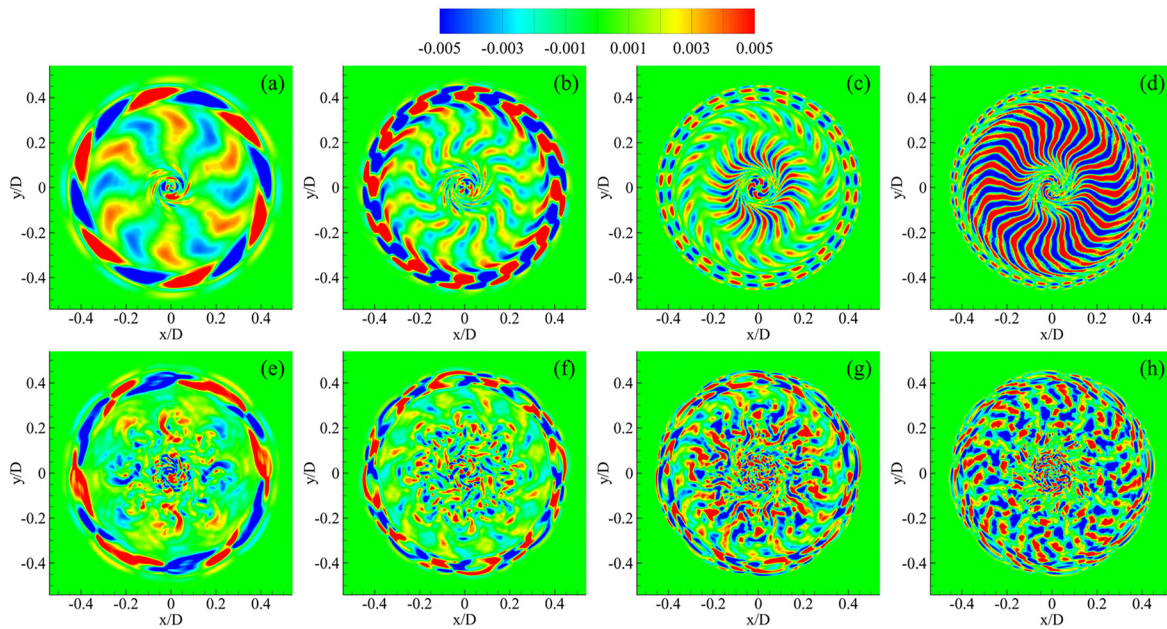


FIG. 22. DMD modes on 0.7 D transverse plane of DP and PJP wake fields: (a)–(d) modes 1–4 of DP, and (e)–(h) modes 1–4 of PJP.

of PJP still develop in a chaotic manner in this plane. Some small-scale modal structures fused into large-scale structures, as seen from mode 1. Conversely, some large-scale structures also decomposed into smaller ones accompanied by radial diffusion, and some of them completely dissipated by viscous effects, as evident from modes 2–4.

Finally, several special modes that play a dominant role in the energy spectrum of different transverse planes in DP case are extracted and analyzed. The modal structures of modes A to D that have been labeled in the energy spectrum are shown in Fig. 25, where the mode A is extracted from the vorticity field of

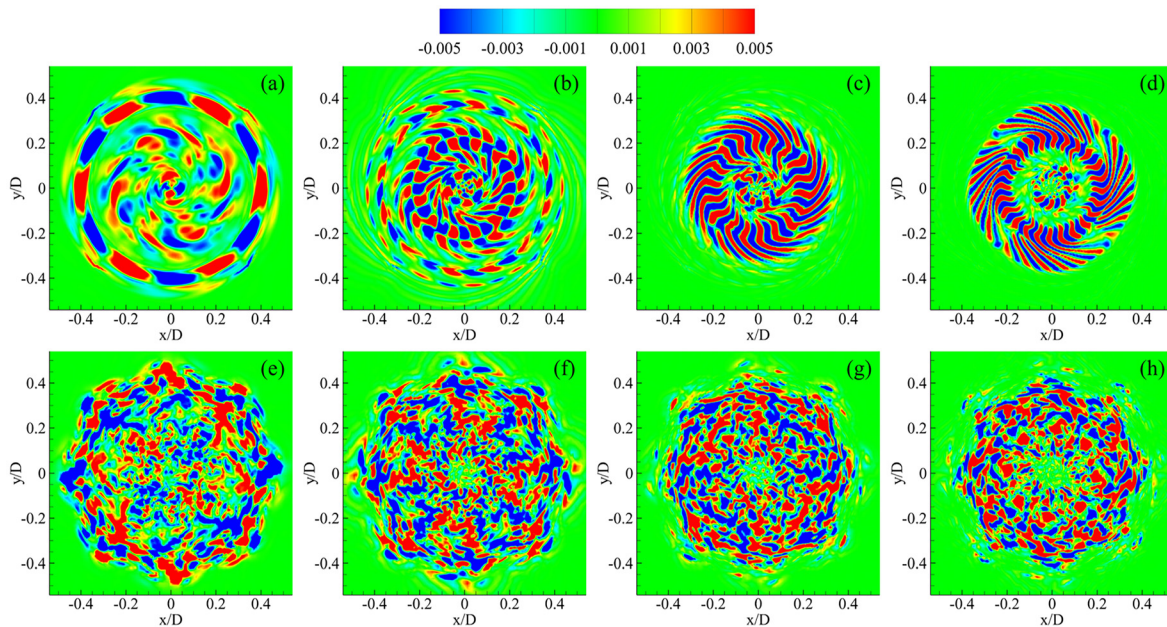


FIG. 23. DMD modes on 1.5D transverse plane of DP and PJP wake fields: (a)–(d) modes 1–4 of DP and (e)–(h) modes 1–4 of PJP.

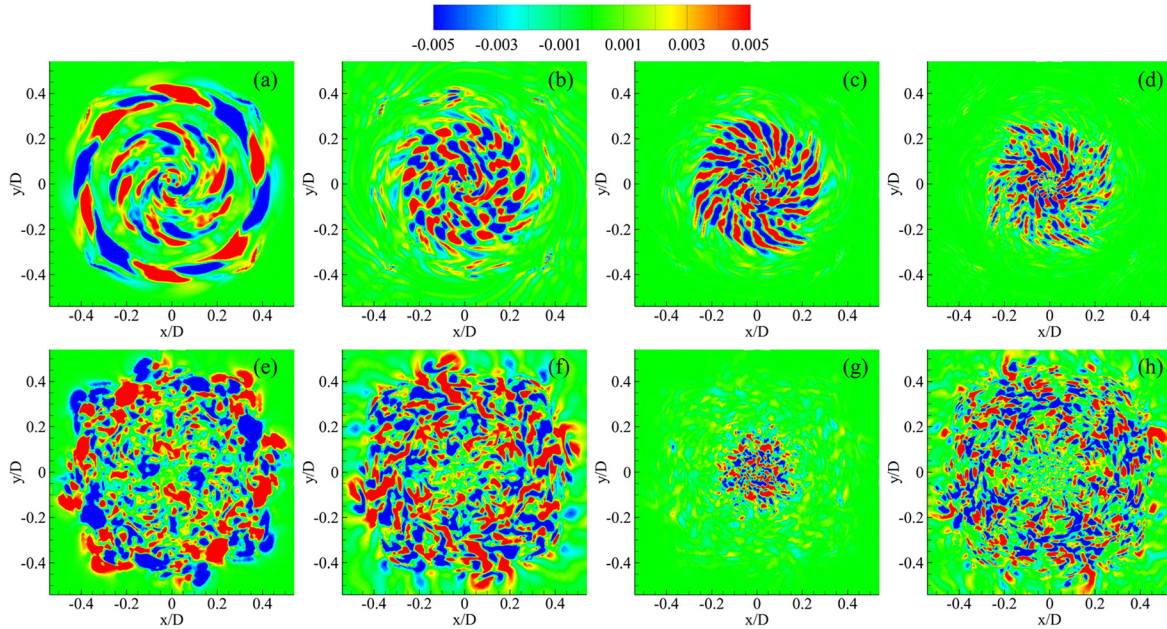


FIG. 24. DMD modes on 2.3D transverse plane of DP and PJP wake fields: (a)–(d) modes 1–4 of DP and (e)–(h) modes 1–4 of PJP.

0.7D plane with a characteristic frequency $f=283.7$ Hz, the modes B and C are extracted from 1.5D plane with characteristic frequencies $f=58$ Hz and $f=195$ Hz, the mode D is obtained from 2.3D plane with a characteristic frequency $f=47.8$ Hz. It is evident in Fig. 25 that the modal structures of the four special modes are mainly concentrated in the hub vortex region. This indicates that the axial evolution of the hub vortex plays an important role in the wake dynamics of DP in this study, and dominates the energy spectrum characteristics of different transverse planes. In addition, it is found that the dominant mode frequency of the hub vortex shifts from the higher frequency $f=283.7$ Hz to the lower frequency $f=47.8$ Hz along the streamwise direction, which is more related to the energy transfer process in the propeller wake field.⁵

V. CONCLUSION

In this study, the delayed detached eddy simulations are carried out to investigate the wake dynamics of DP and PJP, with the purpose of evaluating the effects of pre-swirl stator and stator–rotor interaction on the evolution of wake coherent structures and destabilization mechanisms of a PJP system. The DP model is obtained by removing the pre-swirl stator from the PJP in order to ensure comparable results. The hydrodynamic loading tests and flow field visualization are conducted for the PJP system in open water conditions. Numerical results are qualitatively and quantitatively verified based on experimental data and demonstrated reasonable accuracy. Then, the wake field characteristics of the DP and PJP models are comparatively analyzed by means of flow physical quantities analysis, three-dimensional vortex structure identification, and modal analysis technique.

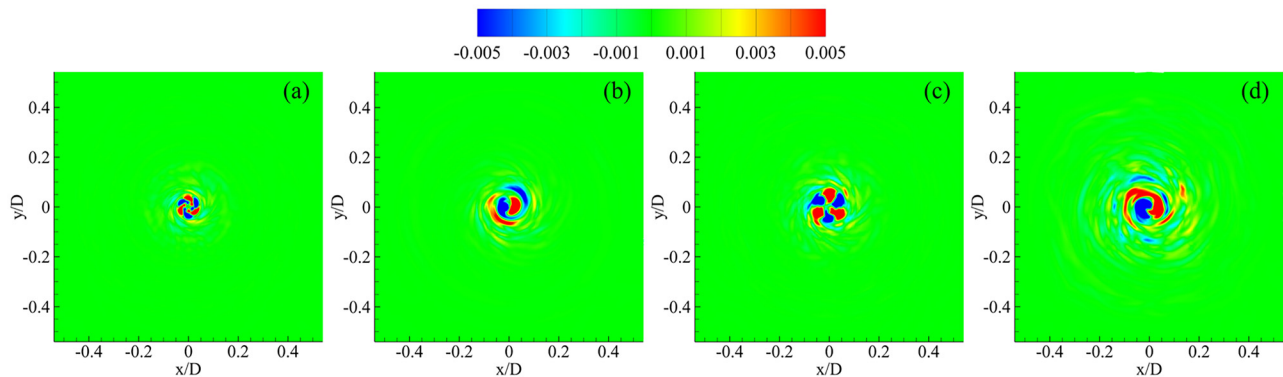


FIG. 25. Four special DMD modes on different transverse planes of DP wake field: (a) mode A, (b) mode B, (c) mode C, and (d) mode D.

05 April 2024 07:28:53

The existence of a pre-swirl stator increases the hydrodynamic loading of the PJP system by optimizing the rotor incoming flow, meanwhile, it also contributes to the instability of the wake field. The trailing vortices induced by the stator are cutoff by the rotating rotor to form numerous small-scale vortex filaments, which further mutually interact with the rotor trailing vortices and hub vortex, accelerating their diffusion and viscous dissipation along the radial and axial directions. The TLV plays an important role in the wake dynamics of both DP and PJP models. Compared with DP, the stator-rotor interaction causes the TLV to experience sinusoidal fluctuations before leaking out of the duct. The splitting effect of the stator on the fluid propagates to the wake field, which induces the TLV secondary vortices and destroys the continuity of the TLV spiral topology, thereby accelerating its instability. The negative pre-swirl of the stator largely absorbs the circumferential velocity in the wake field and moderates the spiral behavior of the TLV.

The dominant flow structures and mutual interaction processes can be captured by modal features at different characteristic frequencies obtained from DMD analysis. The PJP wake field is dominated by modal features at f_{BPF} and its multiples, while some special modes related to hub vortex evolution contribute significantly to the wake field characteristics of DP. The dominant structure of the TLV is identified by the mode 1 located at f_{BPF} . The mutual interaction between DSV and TLV and the interaction process between the rotor wake and adjacent TLV are characterized by the mode 2 at $2f_{BPF}$. The viscous dissipation of the rotor wake along the axial direction is identified by the modes 3 and 4. Compared to other interaction mechanisms, the multi-modulation of stator on the wake field dominates the wake dynamics and the underlying instability mechanism of the PJP.

ACKNOWLEDGMENTS

This work was financially supported by National Natural Science Foundation of China (Grant No. 51979125), Jiangsu Provincial Science Fund for Distinguished Young Scholars (Grant No. BK20211547), and Innovation Project for Postgraduates of Jiangsu Province (Grant No. KYCX21_3346). The authors would like to thank the China Scholarship Council (CSC No. 202208320309) for support of this research.

AUTHOR DECLARATIONS

Conflict of Interest

The authors have no conflicts to disclose.

Author Contributions

Xutao Zhao: Investigation (lead); Methodology (lead); Software (lead); Validation (lead); Writing – original draft (lead); Writing – review & editing (equal). **Xi Shen:** Methodology (equal); Validation (equal); Writing – review & editing (equal). **Linlin Geng:** Validation (equal); Writing – review & editing (equal). **Desheng Zhang:** Funding acquisition (lead); Resources (equal); Supervision (equal); Writing – review & editing (equal). **B. P. M. (Bart) van Esch:** Supervision (equal); Writing – review & editing (equal).

DATA AVAILABILITY

The data that support the findings of this study are available from the corresponding authors upon reasonable request.

REFERENCES

- P. Kumar and K. Mahesh, "Large eddy simulation of propeller wake instabilities," *J. Fluid Mech.* **814**, 361 (2017).
- S. Sarmast, R. Dadfar, R. F. Mikkelsen, P. Schlatter, S. Ivanell, J. N. Sørensen, and D. S. Henningson, "Mutual inductance instability of the tip vortices behind a wind turbine," *J. Fluid Mech.* **755**, 705 (2014).
- V. L. Okulov and J. N. Sørensen, "Stability of helical tip vortices in a rotor far wake," *J. Fluid Mech.* **576**, 1 (2007).
- K. Kan, H. Li, and Z. Yang, "Large eddy simulation of turbulent wake flow around a marine propeller under the influence of incident waves," *Phys. Fluids* **35**(5), 055124 (2023).
- M. Felli, R. Camussi, and F. Di Felice, "Mechanisms of evolution of the propeller wake in the transition and far fields," *J. Fluid Mech.* **682**, 5 (2011).
- A. Di Mascio, R. Muscari, and G. Dubbioso, "On the wake dynamics of a propeller operating in drift," *J. Fluid Mech.* **754**, 263 (2014).
- D. Qin, Q. Huang, G. Pan, L. Chao, Y. Luo, and P. Han, "Effect of the odd and even number of blades on the hydrodynamic performance of a pre-swirl pump-jet propulsor," *Phys. Fluids* **34**, 035120 (2022).
- H. Li, Q. Huang, G. Pan, and X. Dong, "Wake instabilities of a pre-swirl stator pump-jet propulsor," *Phys. Fluids* **33**, 085119 (2021).
- Y. Zhang, J. Han, B. Huang, D. Zhang, and D. Wu, "Excitation force on a pump-jet propeller: The effect of the blade number," *Ocean Eng.* **281**, 114727 (2023).
- S. E. Widnall, "The stability of a helical vortex filament," *J. Fluid Mech.* **54**, 641 (1972).
- J. N. Sørensen, "Instability of helical tip vortices in rotor wakes," *J. Fluid Mech.* **682**, 1 (2011).
- R. Muscari, A. Di Mascio, and R. Verzicco, "Modeling of vortex dynamics in the wake of a marine propeller," *Comput. Fluids* **73**, 65 (2013).
- H. Li, Q. Huang, G. Pan, and X. Dong, "The transient prediction of a pre-swirl stator pump-jet propulsor and a comparative study of hybrid RANS/LES simulations on the wake vortices," *Ocean Eng.* **203**, 107224 (2020).
- L. Wang, T. Wu, J. Gong, and Y. Yang, "Numerical simulation of the wake instabilities of a propeller," *Phys. Fluids* **33**, 125125 (2021).
- S. Shi, W. Tang, and X. Huang, "Wake flow characteristics and unsteady performance of a pump-jet propulsor under hull condition," *Phys. Fluids* **34**, 127110 (2022).
- A. Posa, R. Brogna, M. Felli, M. Falchi, and E. Balaras, "Characterization of the wake of a submarine propeller via large-eddy simulation," *Comput. Fluids* **184**, 138 (2019).
- J. Gong, J. Ding, and L. Wang, "Propeller-duct interaction on the wake dynamics of a ducted propeller," *Phys. Fluids* **33**, 074102 (2021).
- J. Gong, C.-y. Guo, D.-g. Zhao, T.-c. Wu, and K.-w. Song, "A comparative DES study of wake vortex evolution for ducted and non-ducted propellers," *Ocean Eng.* **160**, 78 (2018).
- Q. Zhang and R. K. Jaiman, "Numerical analysis on the wake dynamics of a ducted propeller," *Ocean Eng.* **171**, 202 (2019).
- H. Yu, N. Duan, H. Hua, and Z. Zhang, "Propulsion performance and unsteady forces of a pump-jet propulsor with different pre-swirl stator parameters," *Appl. Ocean Res.* **100**, 102184 (2020).
- F. Z. Li, G. S. Liu, Q. G. Huang, G. C. Sun, G. Pan, and D. H. Qin, "Influence of asymmetric pre-whirl stator spacing on unsteady characteristics of pump-jet propulsor," *Ocean Eng.* **273**, 113896 (2023).
- F. Li, Q. Huang, G. Sun, G. Pan, H. Li, and C. Bai, "Numerical simulation of the flow field and radiation noise from a pump-jet propulsor under various stator pre-whirl angles," *Appl. Ocean Res.* **135**, 103558 (2023).
- F. Magionesi, G. Dubbioso, R. Muscari, and A. Di Mascio, "Modal analysis of the wake past a marine propeller," *J. Fluid Mech.* **855**, 469 (2018).
- H. Shi, T. Wang, M. Zhao, and Q. Zhang, "Modal analysis of non-ducted and ducted propeller wake under axis flow," *Phys. Fluids* **34**, 055128 (2022).

- ²⁵T. Wang, H. Shi, M. Zhao, and Q. Zhang, "Effects of a nozzle on the propeller wake in an oblique flow using modal analysis," *J. Fluid Mech.* **959**, A14 (2023).
- ²⁶C. Sun, T. Tian, X. Zhu, O. Hua, and Z. Du, "Investigation of the near wake of a horizontal-axis wind turbine model by dynamic mode decomposition," *Energy* **227**, 120418 (2021).
- ²⁷K. Taira, S. L. Brunton, S. T. M. Dawson, C. W. Rowley, T. Colonius, B. J. McKeon, O. T. Schmidt, S. Gordeyev, V. Theofilis, and L. S. Ukeiley, "Modal analysis of fluid flows: An overview," *AIAA J.* **55**, 4013 (2017).
- ²⁸C. W. Rowley and S. T. M. Dawson, "Model reduction for flow analysis and control," *Annu. Rev. Fluid Mech.* **49**, 387 (2017).
- ²⁹J. L. Lumley, *Stochastic Tools in Turbulence* (Courier Corporation, 2007).
- ³⁰P. J. Schmid, "Dynamic mode decomposition of numerical and experimental data," *J. Fluid Mech.* **656**, 5 (2010).
- ³¹P. J. Schmid, D. Violato, and F. Scarano, "Decomposition of time-resolved tomographic PIV," *Exp. Fluids* **52**, 1567 (2012).
- ³²Y. Zhi, R. Qiu, R. Huang, and Y. Wang, "Dynamic mode decomposition and reconstruction of the transient propeller wake under a light loading condition," *Ocean Eng.* **269**, 113532 (2023).
- ³³C. Sun and L. Wang, "Modal analysis of propeller wake dynamics under different inflow conditions," *Phys. Fluids* **34**, 125109 (2022).
- ³⁴L. Wang, X. Liu, N. Wang, and M. Li, "Modal analysis of propeller wakes under different loading conditions," *Phys. Fluids* **34**, 065136 (2022).
- ³⁵L. Wang, X. Liu, and T. Wu, "Modal analysis of the propeller wake under the heavy loading condition," *Phys. Fluids* **34**, 055107 (2022).
- ³⁶P. R. Spalart, S. Deck, M. L. Shur, K. D. Squires, M. K. Strelets, and A. Travin, "A new version of detached-eddy simulation, resistant to ambiguous grid densities," *Theor. Comput. Fluid Dyn.* **20**, 181 (2006).
- ³⁷I. B. Celik, U. Ghia, P. J. Roache, and C. J. Freitas, "Procedure for estimation and reporting of uncertainty due to discretization in CFD applications," *J. Fluids Eng.* **130**, 078001 (2008).
- ³⁸X. Zhao, X. Shen, L. Geng, D. Zhang, and B. P. M. B. van Esch, "Effects of cavitation on the hydrodynamic loading and wake vortex evolution of a pre-swirl pump-jet propulsor," *Ocean Eng.* **266**, 113069 (2022).
- ³⁹D. Qin, Q. Huang, G. Pan, Y. Shi, P. Han, and X. Dong, "Effect of the duct and the pre-swirl stator on the wake dynamics of a pre-swirl pumpjet propulsor," *Ocean Eng.* **237**, 109620 (2021).
- ⁴⁰C. Liu, Y.-S. Gao, X.-R. Dong, Y.-Q. Wang, J.-M. Liu, Y.-N. Zhang, X.-S. Cai, and N. Gui, "Third generation of vortex identification methods: Omega and Liutex/Rortex based systems," *J. Hydrodyn.* **31**, 205 (2019).
- ⁴¹X.-R. Dong, Y.-Q. Wang, X.-P. Chen, Y. Dong, Y.-N. Zhang, and C. Liu, "Determination of epsilon for Omega vortex identification method," *J. Hydrodyn.* **30**, 541 (2018).
- ⁴²H. Nyquist, "Certain topics in telegraph transmission theory," *Trans. Am. Inst. Electr. Eng.* **47**, 617 (1928).
- ⁴³C. E. Shannon, "Communication in the presence of noise," *Proc. IRE* **37**, 10 (1949).